*J. Fluid Mech.* (2025), *vol.* 1008, A18, doi:10.1017/jfm.2025.76

# Laboratory study of the enhanced wave-induced drift of large rectangular floating objects

**Q. Xiao**[1], **M.L. McAllister**[1], **T.A.A. Adcock**[1] **and T.S. van den Bremer**[1,2]

[1]Department of Engineering Science, University of Oxford, Oxford, OX1 3PJ, UK

[2]Department of Civil Engineering and Geosciences, TU Delft, Stevinweg 1, Delft, 2628 CN, The Netherlands

**Corresponding author:** Q. Xiao, qx7402@princeton.edu

(Received 22 December 2023; revised 1 November 2024; accepted 10 January 2025)

Surface gravity waves induce a drift on objects floating on the water's surface. This study presents laboratory experiments investigating the drift of large two-dimensional floating objects on deep-water, unidirectional, regular waves, with wave steepness ranging from 0.04 to 0.31 ($0.04 < ka_w < 0.31$, where $k$ is the wavenumber and $a_w$ the wave amplitude). The objects were carefully designed to have a rectangular cross-section with a constant aspect ratio; their size varied from 2.6 % to 27 % of the incident wavelength. We observed Lagrangian behaviour for small objects. Small and large objects exhibited fundamentally different drift behaviour at high compared with low wave steepness, with a regime shift observed at a certain size and wave steepness. The scaling of object drift with steepness depends on the relative size of the object. For small objects, drift scales with steepness squared, whereas drift becomes a linear function of steepness as the object size increases. For objects that are relatively large but smaller than 13–16% of a wavelength (low to high steepness), we provide experimental evidence supporting the mechanisms of drift enhancement recently identified by Xiao *et al.* (*J. Fluid Mech.*, vol. 980, 2024, p. A27) and termed the 'diffraction-modified Stokes drift'. This enhanced drift behaviour, compared with the theoretical Stokes drift for infinitely small fluid parcels, is attributed to changes in the objects' oscillatory motion and local wave amplitude distribution (standing wave pattern) due to the presence of the object. In the case of larger objects, similar to Harms (*J. Waterw. Port Coast. Ocean Eng.*, vol. 113(6), 1987, pp. 606–622), we relate the critical size at which drift is maximised to their vertical bobbing motion. We determine the domain of validity for both Stokes drift and the diffraction-modified Stokes drift model of Xiao *et al.* (*J. Fluid Mech.*, vol. 980, 2024, A27) in terms of relative size and wave steepness and propose an empirical parametrisation based on our experimental data.

**Key words:** wave–structure interactions, surface gravity waves

---

## 1. Introduction

The assessment of mass transport in the ocean plays a crucial role in determining the migration of sediments, pollutants (Iwasaki *et al.* 2017; Dobler *et al.* 2019), tracking buoys (Nath 1978; DeBok & Roehrig 1981; Wilson 1982; Tanizawa, Minami & Imoto 2001), ice floes (Arikainen 1972; Perrie & Hu 1997; Meylan *et al.* 2015), as well as trajectory forecasting for search and rescue operations (Röhrs *et al.* 2012; Breivik *et al.* 2013). The recent surge in interest in this topic is driven by the alarming increase in plastic pollution, which requires effective management and clean-up, beginning with an improved understanding of their global transport patterns (Law *et al.* 2010; Eriksen *et al.* 2014; Van Sebille *et al.* 2015; Law 2017; Van Sebille *et al.* 2020). In this study, we investigate the drift motion of large floating objects induced by surface gravity waves.

### 1.1. *Reasons for enhanced drift*

The orbit of a fluid particle in waves is not fully closed over a wave cycle, resulting in a net drift in the direction of wave propagation known as Stokes drift (Stokes 1847). To study the transport of floating objects, several studies have superimposed the Stokes drift onto the Eulerian current field obtained from ocean general circulation models or observations (see Van Sebille *et al.* (2020) for a review). There are three reasons why this approach may not result in a correct prediction of the drift of floating objects in the real ocean. First, this approach ignores the modification of the Eulerian-mean flow by the surface waves: on the rotating Earth, the Stokes–Coriolis force drives an Eulerian mean. This so-called Ekman–Stokes flow needs to be added to the Stokes drift to properly estimate the wave-induced Lagrangian-mean flow, which is the flow responsible for transporting objects floating on the ocean surface (Higgins, Vanneste & van den Bremer 2020*b*). On the time and spatial scales associated with typical laboratory experiments, this Ekman–Stokes flow does, of course, not arise. Second, it has been shown that the drift at the surface of a breaking wave is much larger than the prediction of classical Stokes drift for non-breaking waves (Deike, Pizzo & Melville 2017), as confirmed in experiments (Lenain, Pizzo & Melville 2019; Sinnis *et al.* 2021), and breaking may make a significant contribution to the Lagrangian drift of realistic wave fields (Pizzo, Melville & Deike 2019). In the context of irregular waves, Eeltink *et al.* (2023) have recently proposed a stochastic differential equation that uses a Brownian motion to capture the non-breaking drift-diffusion effect associated with a random non-breaking sea state and a compound-Poisson process to capture the rapid jumps in particle position that take place during wave breaking. Third, unlike an idealised fluid particle (that is, a perfect Lagrangian tracer), floating marine objects exhibit significant variations in size, which can lead to non-Lagrangian drift behaviour (Nath 1978; Santamaria *et al.* 2013; Ren *et al.* 2015; Calvert *et al.* 2021; DiBenedetto, Clark & Pujara 2022).

This non-Lagrangian drift behaviour is the subject of the present paper. Studies that have examined the drift of non-Lagrangian particles or 'objects' can be classified into those that ignore the disturbance of the wave field by the object and those that take this disturbance into account. Typically, the effect of the object on the wave field can be neglected when the relative size of the object (characterised by $l/\lambda$, the ratio of the object's characteristic dimension $l$ to the incident wavelength $\lambda$) is smaller than 0.2 (Isaacson 1979).

### 1.2. *Drift of objects that do not disturb the wavefield*

Beginning with studies that have ignored the disturbance of the wave field by the object and focusing on fully submerged particles, Eames (2008) and Santamaria *et al.* (2013) used the Maxey–Riley equations (Maxey & Riley 1983) to examine how far slightly positively or negatively buoyant objects are transported by regular waves as they either rise to the free surface or sink. Santamaria *et al.* (2013) predicted that positively buoyant objects in deep-water waves experience an increase in drift owing to their inertia (see DiBenedetto *et al.* (2022) for an extension to finite depth). Also considering fully submerged objects, DiBenedetto & Ouellette (2018) showed that non-spherical objects have a preferential orientation under waves, confirming this result numerically (DiBenedetto & Ouellette 2018) and experimentally (DiBenedetto, Koseff & Ouellette 2019), but not examining the effect of the object's inertia or its modified drift. Even without direct modification of the drift, the orientation changes the drag on slightly negatively buoyant objects, which results in objects of different shapes being transported different distances before 'raining out' (DiBenedetto, Ouellette & Koseff 2018). Taking a similar approach, Pujara & Thiffeault (2023) have shown that wave action reduces the vertical dispersion of particles but increases horizontal dispersion.

Turning to floating objects, but still ignoring the disturbance of the wave field they cause, theoretical models that apply forces derived from the wave field onto a moving object, assuming the wave field is unaffected by the presence of the object itself (e.g. through Morison's equation (Morison, Johnson & Schaaf 1950)) are thus commonly used to study the drift motion of small objects (Rumer, Crissman & Wake 1979; Shen & Ackley 1991; Shen & Zhong 2001; Grotmaack & Meylan 2006; Huang, Huang & Law 2016). Calvert *et al.* (2021) used a perturbation expansion in wave steepness to derive a closed-form solution for the enhanced drift of a floating sphere, extending the models of Rumer *et al.* (1979) and Huang *et al.* (2016). Calvert *et al.* (2021) attributed the enhanced drift to two physical mechanisms: the increased vertical oscillatory (linear) motion of the floating sphere and the (viscous) drag-induced phase difference between the motion of the inertial sphere and that of an idealised Lagrangian particle, giving rise to a net horizontal component of the buoyancy force when averaged over a wave cycle.

### 1.3. *Drift of objects that do disturb the wavefield*

In those models that do take the disturbance to the wave field by the (floating) object into account, the object's surfaces are often treated as part of the boundary of the fluid domain, and the problem is approached based on potential-flow theory (Haskind 1946; Faltinsen 1993; Newman 2018). Apart from the (linear) oscillatory (unsteady) exciting forces leading to (linear) oscillatory motion, objects exposed to waves also experience steady (i.e. wave-averaged) nonlinear forces, giving rise to a slow drift motion in the direction of wave propagation. This steady second-order force is often referred to as the (mean) drift force and affects the trajectories of objects in waves (Suyehiro 1924; Watanabe 1938; Havelock 1942; Skejic & Faltinsen 2008). There are three main approaches to calculating the drift force: the near-field formulation (Pinkster & Hooft 1976; Pinkster & Van Oortmerssen 1977), which solves for the second-order disturbance in the near field by direct integration of pressure on the surface of the wetted body; the far-field formulation (Newman 1967), which is derived from conservation of momentum and thus sets the change in momentum (flux) of the fluid equal to the mean force acting on the object; and the middle-field formulation (Chen 2007), which applies momentum conservation to a fluid control volume and introduces control surfaces around the body.

All three approaches focus on the calculation of a force when the object's drift speed is zero and/or on the calculation of motion when an object is moored. They do not (directly) predict the drift of a freely floating object. Typically, the objects considered are three-dimensional with relatively large sizes, often comparable to the wavelength. Moreover, few studies (e.g. Newman 1967) have examined cases in following waves where objects are travelling in the direction of wave propagation (cf. ships), characterised by heading angles of 0° (most of the cases are in oblique waves or head waves). A floating object travelling with a constant velocity on the surface of otherwise calm water experiences a non-viscous (i.e. potential-flow) drag, reflecting the energy required to push the fluid out of the way of the object, known as the wave-making resistance (Michell 1898; Havelock 1909). In principle and analogously to this wave-making resistance, the so-called wave drift damping force (Nossen, Grue & Palm 1991; Aranha 1994), which acts on a slowly drifting object, could balance the drift force discussed above, perhaps aided by a further viscous or turbulent drag term in realistic flows, leading to force equilibrium and resulting in steady drift motion. However, the authors are unaware of existing work that uses such an equilibrium of drift and drift damping forces to obtain estimates of the (enhanced) drift of floating objects, and note that the required analysis would not be straightforward based solely on existing work (e.g. Nossen *et al.* 1991; Aranha 1994).

To consider the effect of diffraction on the wave-induced drift of freely floating objects Xiao *et al.* (2024) used a two-dimensional (2-D) hybrid numerical solver, which deals with both viscosity and wave–body interaction, to predict significant drift enhancement of large (5–10 % of the wavelength) floating rectangular boxes. The drift enhancement was explained in small part by the effect of viscosity (as by Calvert *et al.* 2021), but in large part by the standing wave pattern generated by the presence of the (oscillating and drifting) object in the wave field. To explain their numerical results, Xiao *et al.* (2024) derived a 'diffraction-modified Stokes drift' akin to Stokes (1847), but based on the combination of incident, diffracted and radiated wave fields, which are based on potential-flow theory and obtained using the boundary element method (BEM). This 'diffraction-modified Stokes drift' could explain both qualitatively and quantitatively the increase in drift predicted by the hybrid numerical model.

### 1.4. *Relative object size and steepness: previous experimental studies*

Experimental investigations of the wave-induced motion and drift of floating objects have been conducted for nearly half a century. Table 1 provides a summary of relevant experimental studies, including the present paper. This table shows that the drift of an object depends on its relative size. The drift of very small objects is equal to the theoretical Stokes drift. However, as the objects become larger, enhanced drift is observed (we refer to drift as 'enhanced' in this paper when it is larger than the theoretical Stokes drift). Nath (1978) reported Lagrangian drift behaviour for small discs and spheres on regular waves but found enhanced drift for larger objects with deep drafts (such as spar-type buoy drifters) in low wave steepness. Measurements by Murray, Guy & Muggeridge (1983) suggested that the maximum horizontal drift attained by floating spheres differs substantially from that of a water particle only when $l/\lambda >$ 12.5 %. Similar conclusions were drawn by Alsina, Jongedijk & van Sebille (2020) regarding the drift of floating spherical particles with $l/\lambda$ ranging from 0.1 % to 1.4 %, which were not enhanced. Calvert *et al.* (2021) suggested that the drift of a sphere increases with its relative size, and enhanced drift was found for objects as small as $l/\lambda = 6\%$. Le Boulluec, Forest & Mansuy (2008) found that, regardless of shape, the drift velocity increases with relative size of the object $l/\lambda$, considering a range of relative size from 6% to 50%.

| **2-D:** | Third dimension | $l/\lambda$ [%] | $h/l$ | Shape | $\rho$ [kg/m$^3$] | $kd$ | $ka_w$ | Wave type |
|---|---|---|---|---|---|---|---|---|
| Harms (1987) | 6 mm gap | 5.8–106.5 | 0.01–0.68 | Rectangular box | 920 | >1.7 | 0.06–0.30 | R |
| Tanizawa *et al.* (2001) | 10 cm gap | 12.7–63.6 | 0.56 | Rectangular box | 887 | 0.8–5 | 0.03–0.20 | R+IR |
| Huang and Law (2013) | 5 cm gap | 61.0–308.0 | 0.01–0.05 | Rectangular box | 720 | 2.6–12.9 | 0.04–0.32 | R |
| He *et al.* (2016) | 2 cm gap | 9.2–30.4 | 0.67 | Rectangular box | 500 | 0.7–2.5 | 0.04–0.30 | R |
| Present paper | Plastic bearings | 2.6–27.1 | 0.67 | Rectangular box, sphere | 636 | 2.8–4.1 | 0.03–0.32 | R |
| **3-D:** | | | | | | | | |
| Nath (1978) | — | 0.2–176.5 | 0.17,0.23,1 | Sphere, disk and deep-draft buoy | >= 500 | 1.1–14.1 | >0.02 | R |
| Murray *et al.* (1983) | — | 11–53 | — | Cylinder, sphere and cube | 900 | 2.6–12.3 | 0.02–0.06 | R+WG |
| Tanizawa *et al.* (2001) | — | 3.0–60.8 | 1.00 | Spherical buoy | >500 | >2.8 | 0.06–0.4 | R+IR |
| Le Boulluec *et al.* (2008) | — | 10.0–100.0 | 0.24–0.50 | Rectangular container and cylinder | 175–954 | >4.0 | — | R+IR |
| Huang *et al.* (2011) | — | 12.8–15.8 | 0.15, 0.23 | Square, circular and elliptical plates | 960 | 3.2–4.0 | 0.04–0.15 | R |
| Meylan *et al.* (2015) | — | 8.0–80.0 | 0.04 | Thin plastic disk | 891 | 1.0–10.1 | >0.006 | R |
| Alsina *et al.* (2020) | — | 0.1–1.4 | 1.00 | Spherical particles | 760–1340 | 0.3–3.0 | 0.06–0.22 | R |
| Calvert *et al.* (2021) | — | 1.9–5.1 | 1.00 | Sphere | 508–809 | 3.1 | 0.1 | WG |

Table 1. Summary of previous laboratory studies of wave-induced drift of freely floating objects on waves. Some values not explicitly provided in the cited papers were obtained from digitised figures or estimated using the linear dispersion relationship. In 2-D experiments, the 'third dimension' shows the approach used to ensure the experiment's 2-D nature. $l$ represents the length of the object in the direction of wave propagation, $\lambda$ the wavelength, $h$ the height of the object, $\rho$ the density of the object, $k$ the wavenumber, $d$ the water depth, and $a_w$ the wave amplitude. The wave types R, IR, and WG correspond to regular waves, irregular waves, and wave groups, respectively.

Drift behaviour is also influenced by the incident wave steepness. Tanizawa *et al.* (2001) reported Lagrangian drift behaviour for a spherical buoy with a relative size of $l/\lambda = 6\%$ at low wave steepness, while enhanced drift was observed for all objects with $l/\lambda > 10\%$ across various wave steepnesses. They proposed that, for small objects, drift is proportional to the square of the wave steepness, and as the object size increases, drift gradually becomes linearly proportional to the wave steepness. Huang, Law & Huang (2011) also found enhanced drift behaviour for objects with $l/\lambda$ ranging from 12.8% to 15.8%, and the magnitude of this drift enhancement increased with wave steepness.

### 1.5. *3-D versus 2-D objects*

All the experimental studies mentioned above are three-dimensional (3-D), meaning that while the wave conditions may be unidirectional, the objects do not span the entire wave crest. The scarcity of 2-D studies can be attributed to the greater experimental difficulty in designing objects that are truly 2-D and capable of moving freely in a wave tank, especially for very small objects. Additionally, lateral variations in surface elevation for unidirectional waves pose challenges. Previous 2-D studies have typically used models that occupy the full width of the flume, with a small gap between the walls and models to ensure free movement.

Harms (1987) conducted systematic 2-D laboratory measurements on the drift of ice floes, which exhibit significant variations in size. He proposed an empirical formula for wave-induced drift based on the ratio of wave period to the object's natural roll period, wave steepness, and the length of the floe. His formula suggests that the object's drift changes with its relative size, and there is a critical size, the value of which depends on the object's aspect ratio (typically approximately $l/\lambda = 50\%$ for an object with $h/l = 0.08$, where $h$ is its height and $l$ its length, and density $\rho = 920\,\mathrm{kg\,m^{-3}}$). When the object is smaller than the critical size, the drift increases approximately linearly with its relative size. However, when the object is larger than the critical size, the drift decreases substantially and nonlinearly with further increases in relative size. The value of this critical size does not vary significantly with wave steepness. For objects with different aspect ratios (but the same density), when the relative size is smaller than the critical size for all objects, the drift increases as the submergence increases with increasing $h/l$. This finding is consistent with the measurements of Huang & Law (2013), which focused on relatively large objects with $l/\lambda > 60\%$. Tanizawa *et al.* (2001) and He, Ren & Qiu (2016) also observed enhanced drift for intermediate sizes ($l/\lambda$ ranging from 10 % to 60 %), and the relationship between drift velocity and wave steepness shifted from a quadratic to a linear relationship. Specifically, He *et al.* (2016) found that the ratio of the magnitudes of the quadratic components to the linear components shifted from 10 to 0 for objects ranging from $l/\lambda = 9\%$ to 30%.

### 1.6. *Present paper*

This paper reports the results from laboratory experiments examining the enhanced wave-induced drift, large, 2-D, rectangular floating objects. We set out to make two contributions.

First, this paper aims to observe and study experimentally the mechanism for enhanced drift described by the diffraction-modified Stokes drift theory proposed by Xiao *et al.* (2024). To do so, we perform a comparison with the numerical results of Xiao *et al.* (2024). While documenting the dependence of enhanced drift on different parameters, the experimental literature surveyed above has not examined the mechanism(s) explaining the drift enhancement or the relationships between drift velocity and the oscillatory motion of objects, nor has it examined the surface elevation in the vicinity of the object. We aim to do this here.

Second, we explore a gap in the parameter space that the existing literature has left open. To the best of the authors' knowledge, the drift behaviour of objects with relative sizes ranging from $l/\lambda < 6\%$ to $l/\lambda = 27\%$ has not been examined in 2-D experiments previously. In an effort to address this gap and explore object sizes ranging from very small to intermediate size, near or crossing the critical size reported by Harms (1987), we conduct 2-D laboratory experiments investigating the drift behaviour of objects with relative sizes in the range $l/\lambda = 2.6$–$27\%$ in regular deep-water waves. In the ocean, relative size depends on both the size of the litter and the wavelength. On the one hand, pollutants in the ocean greatly vary in size. While most of the litter is small, such as microplastics (<5 mm) (Setälä *et al.* 2014; Cózar *et al.* 2014), there is also large litter, such as wreckage of vessels and ships, which can be tens of meters in length (Carlton *et al.* 2018). On the other hand, typical ocean wavelength consists of scales from 10 cm to 1 km (Lefevre & Cotton 2001; Toffoli & Bitner-Gregersen 2017). As a result, our experiments cover the range from tiny pieces of litter in long waves to large debris in shorter waves.

In this paper, we have chosen to perform experiments with 2-D objects (i.e., objects spanning the entire regular wave crest) for two reasons. Most importantly, 2-D experiments allow a mechanism that probably also occurs in 3-D, but is strongest in 2-D to be isolated, namely the diffraction-modified Stokes drift of Xiao *et al.* (2024), which is proposed in a 2-D context therein. Secondly, while most real-world applications are 3-D, specific applications, such as ice floes (Arikainen 1972; EI-Tahan *et al.* 1983; Wadhams 1983; Harms 1987), are distinctly 2-D. Ice floes can take the form of so-called ice edge bands, which are 2-D-like (typically, 10 km in length and 1 km in width (Wadhams 1983)). To ensure two-dimensionality in our experiments, we utilise carefully designed objects equipped with low-friction bearings.

The outline of the paper is as follows. In § 2 we present our experimental method, followed by a brief introduction to the theoretical model of Xiao *et al.* (2024) and the empirical parametrisation of Harms (1987) in § 3. We present our experimental results in § 4, where we also propose a new empirical parametrisation, and compare our experimental results to the theoretical model of Xiao *et al.* (2024) and the empirical parametrisation of Harms (1987). Finally, we draw conclusions in § 5.

## 2. Experimental method

### 2.1. *Wave flume and camera set-up*

Experiments were conducted in the Wave and Current Flume at the University of Oxford, UK. The flume is 10 m long, 1.1 m wide and 1 m deep with working water depth of 0.85 m. Figure 1 provides a diagram of the experimental set-up. Waves were generated using three hinged flap-type wavemakers, located at one end of the flume. At the other end, a wave-absorbing beach was positioned. It is important to note that the flume is not fully closed, and includes pumps and a pipe system for fluid recirculation underneath the flume that can be used to create a current. Although a current was not actively generated in the present experiments, the presence of the pipe system allows fluid recirculation during wave generation, which may influence the Eulerian current in the flume (it does not provide the no-flow boundary condition a closed tank would provide, see § 2.2). To measure wave properties, seven resistance-type wave gauges were distributed along the flume, sampling the surface elevation at a rate of 128 Hz. The gauges were mounted on a steel frame in five rows. The distances of the rows from the wavemaker were as follows: 2.14 m, 4.59 m,

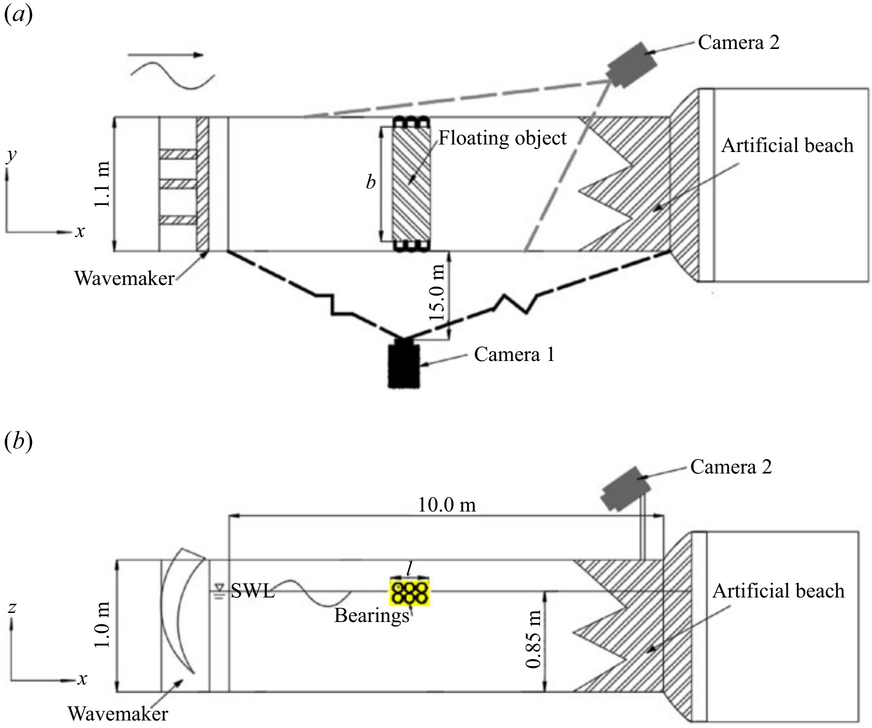

Figure 1. Schematic layout of the wave flume and experimental set-up, indicating the positions of the two cameras, the coordinate system, and the dimensions of the floating object.

6.02 m, 6.32 m, and 6.59 m. Within the rows located at distances of 6.02 m and 6.32 m, two pairs of gauges were placed to assess any lateral variation in the wave field. For each pair of gauges, one was positioned at $y = 0.0$ m (the middle of the flume), while the other was located at $y = 0.275$ m, away from the middle position.

Two E 2–4K Ultra-HD Cinematic Cameras (Z-CAM-E1503) equipped with a Panasonic 12 mm–60 mm digital interchangeable lens were used to measure the movement of the floating objects at 50 frames per second (fps), as depicted in figure 1. Side Camera 1 was positioned at the same height as the still-water level, located 12 m away from the flume. In this configuration, the camera's field of view encompassed the entire length of the flume, and it was horizontally orientated normally to the region of interest including the water surface. Its calibrated camera images were used to measure the drift and oscillatory motion of the floating objects (introduced below) in the $(x, z)$-plane. Top-side Camera 2 was mounted 0.65 m above the still-water level, facing down the wave flume towards the wavemakers. In this set-up, the camera's field of view covered approximately 4 m of the flume length. Camera 2 was specifically used to measure the drift of small yellow balls in the $(x, y)$-plane, as these balls were not visible from the side of the flume due to their size. To ensure proper illumination and consistent lighting conditions for all experiments, three LG-600SC daylight dimmable LED lights (not shown in figure 1) were strategically placed along the length of the flume. These lights illuminated the ends of the objects, which were painted yellow. This illumination scheme also facilitated consistent lighting conditions for subsequent image processing. Optical distortion and pixel scale quantification were achieved by capturing calibration images of a 13 by 10 chequerboard with 50 mm square size using the cameras.

| $f$ (Hz) | $a_w$ (m) | $k$ | $\epsilon = ka_w$ | $kd$ | $\lambda$ (m) | $\Delta a_w$ [%] | $R$ [%] |
|---|---|---|---|---|---|---|---|
| 0.90 | 0.012–0.094 | 3.28 | 0.04–0.31 | 2.79 | 1.91 | 1.27 | 4.19 |
| 1.00 | 0.010–0.079 | 4.03 | 0.04–0.32 | 3.43 | 1.56 | 1.80 | 4.03 |
| 1.05 | 0.009–0.072 | 4.44 | 0.04–0.32 | 3.78 | 1.41 | 2.23 | 6.91 |
| 1.10 | 0.007–0.064 | 4.87 | 0.03–0.31 | 4.14 | 1.29 | 2.58 | 5.33 |

Table 2. Experimental matrix showing the different wave parameters. We have examined a total of 48 wave conditions, combining four different frequencies, each with 12 different wave steepness values ranging from 0.04 to 0.32. The wave steepness interval was 0.02 for $ka$ values between 0.04 and 0.2, and 0.04 for $ka$ values between 0.2 and 0.31. The table includes the following parameters: $f$ (wave frequency), $a_w$ (measured wave amplitude), $k$ (wavenumber), $\epsilon$ (wave steepness), $d$ (water depth), and $\lambda$ (wavelength). The term $\Delta a_w$ represents the lateral variation of the wave amplitude calculated by measuring the wave amplitude using two pairs of gauges positioned at $x = 6.02$ m, $y = 0.0$ m; $x = 6.02$ m, $y = 0.275$ m; $x = 6.32$ m, $y = 0.0$ m; and $x = 6.32$ m, $y = 0.275$ m. The average value across all wave steepness values is reported. $R = a_I/a_R$ refers to the reflection coefficient, which corresponds to the ratio of the incident wave amplitude $a_I$ to the reflected wave amplitude $a_R$.

The parameters describing the waves used in our experiments are presented in table 2. Initially, we conducted experiments with wave gauges installed in the flume, without any objects, to measure the undisturbed wave field. These experiments also allowed us to quantify any unabsorbed reflections and lateral variation of the wave field within the flume. The lateral variation for a single frequency was calculated by determining the relative difference in amplitude measured by the gauges. A reflection analysis based on the methods described by Goda & Suzuki (1976) and Mansard (1980) was performed. As shown in table 2, the lateral variation was found to be low and the wave reflection coefficients were predominantly below 5%, with a maximum value of 10%. For experiments involving the measurement of object motion, the wave gauges were removed. At the beginning of each experiment, the objects were placed in the quiescent flume 1.5 m away from the wavemakers. Waves were then continuously generated until the objects reached a position 1 m from the beach, when the wavemakers were turned off. Recording of the camera and the wavemaker started and ended simultaneously. In cases where large drift speeds were expected (i.e. for large objects in steep waves), the experiments were repeated 2–3 times to ensure a minimum duration of 35 wave periods of data after the drift has reached a quasi-steady state. Following each experiment, a 10-min wait time was observed to allow the flume to settle. To assess the repeatability of our experiments, we conducted additional experiments for four out of the twelve values of input wave steepness ($ka_w = 0.06$, 0.10, 0.20 and 0.32) for each frequency and each object. For these experiments, we performed five repeats, which are analysed in Appendix B.

### 2.2. *Floating objects*

To ensure that our experiments were as close to 2-D as possible, we carefully designed the width $b$ of our floating objects to match that of the flume. To minimise friction between objects and the walls, and to reduce the potential for rotation about the $z$-axis, we installed bearings (Xiros polymer ball transfer unit BB-515-B180-POM) at each end of the objects. Without a certain amount of restraint, smaller objects are prone to twisting caused by small lateral perturbations in the wave-induced forces. The bearings were specifically chosen for their low friction properties. The three dimensions of the objects are denoted as the length $l$ parallel to the $x$-axis, the width $b$ parallel to the $y$-axis and the height $h$ parallel to the $z$-axis, and diagrams showing these dimensions are given in figures 1 and 2, which also depict the layout of the bearings that are fixed to the ends of each object

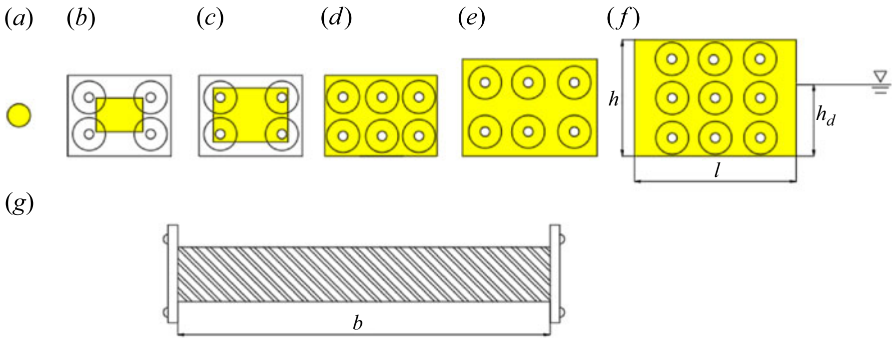

Figure 2. Shapes, bearing layouts, and dimensions of the objects used: (*a*) Object 0 – small yellow polypropylene balls with a diameter of 2 cm and a density of $\rho = 920\,\mathrm{kg\,m^{-3}}$), serving as Lagrangian tracers; (*b*) Object 1– including flange; (*c*) Object 2 – including flange; (*d*) Object 3 – structure with six bearings; (*e*) Object 4 – structure with six bearings; (*f*) Object 5 – structure with nine bearings. (*g*) Top view of the objects with flanges (Objects 1 and &2). The flanges are made of perspex sheet and have a width of 0.15 m, a height of 0.1 m, and thickness of 0.006 m.

| Object numbers | $b$ (m) | $l$ (m) | $h$ (m) | $h_d$ (m) | Number of bearings |
|---|---|---|---|---|---|
| 0 | 0.02 | 0.02 | 0.02 | — | — |
| 1 | 1.066 | 0.050 | 0.033 | 0.021 | 9 |
| 2 | 1.066 | 0.100 | 0.066 | 0.042 | 6 |
| 3 | 1.076 | 0.161 | 0.106 | 0.067 | 6 |
| 4 | 1.076 | 0.201 | 0.131 | 0.084 | 4 |
| 5 | 1.076 | 0.350 | 0.235 | 0.149 | 4 |

Table 3. Object dimensions. Object 0 spherical ball, functioning as a current drogue. The number of bearings indicates the number installed at each end of the object. Objects 1–5 are solid and were constructed from teak wood. The density of these objects is $\rho = 6.36 \times 10^2\,\mathrm{kg\,m^{-3}}$.

(see Appendix A for additional details). The draft (submergence depth) of an object $h_d$ is the vertical distance from its bottom to the free surface when the object is afloat in still water. The values of the dimensions of the objects are provided in table 3. The smallest objects with length $l$ less than 0.16 m (objects 1 and 2), were fitted with 6-mm-thick perspex flanges on their ends to provide enough surface area to mount four bearings and to prevent the objects from rotating about the $z$-axis. To increase the range of relative object sizes $l/\lambda$, alongside varying the size of objects themselves, we also varied the wavelength of the incident waves (see table 4). Figure 3 provides a side and a top view of the smallest and largest objects in the flume.

To determine the strength of Eulerian-mean currents at the surface, we also carried out reference experiments, in which we used small floating balls with a relative size of $l/\lambda = 1.6\%$, as shown in figure 2(a). Previous studies have shown that objects that are this small ($l/\lambda = 1.6\%$) behave as Lagrangian tracers and are thus transported at the speed of the Stokes drift in the absence of Eulerian-mean currents (Harms 1987; Alsina *et al.* 2020; Calvert *et al.* 2021). Thus, their drift corresponds to that of a Lagrangian particle and may be used to determine the strength of Eulerian-mean currents at the surface. In doing so, we further avoid the complexity of directly measuring the Eulerian-mean current (e.g. through

| Object number | 0 | 1 | 1 | 1 | 1 | 2 | 3 | 4 | 3 | 4 | 5 | 5 | 5 | 5 |
|---|---|---|---|---|---|---|---|---|---|---|---|---|---|---|
| $f$ (Hz) | 0.9 | 0.9 | 1.0 | 1.05 | 1.1 | 0.9 | 0.9 | 0.9 | 1.1 | 1.1 | 0.9 | 1.0 | 1.05 | 1.1 |
| $l$ (m) | 0.02 | 0.050 | 0.05 | 0.05 | 0.05 | 0.100 | 0.161 | 0.201 | 0.161 | 0.201 | 0.350 | 0.350 | 0.350 | 0.350 |
| $\lambda$ (m) | 1.91 | 1.91 | 1.56 | 1.41 | 1.29 | 1.91 | 1.91 | 1.91 | 1.29 | 1.29 | 1.91 | 1.56 | 1.41 | 1.29 |
| $l/\lambda$ [%] | 1.1 | 2.6 | 3.2 | 3.6 | 3.9 | 5.2 | 8.4 | 10.5 | 12.5 | 15.6 | 18.3 | 22.4 | 24.8 | 27.1 |

Table 4. Matrix of relative object size $l/\lambda$. For each relative object size, experiments with 12 different values of incident wave steepness were performed.

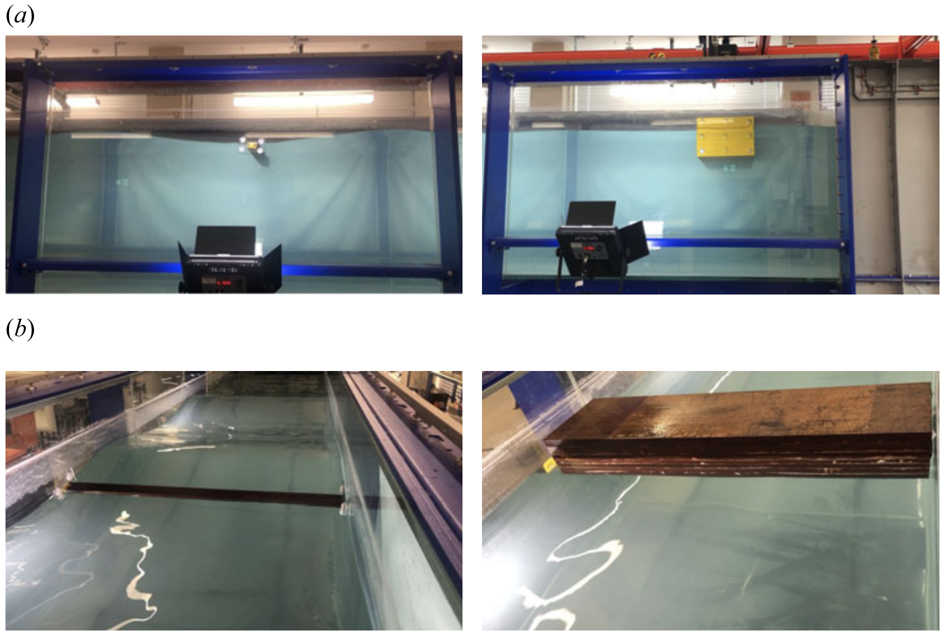

Figure 3. Side and top view of two objects in the wave flume. (*a*) On the left is the small object with $l = 0.05$ m, and on the right is the large object with $l = 0.35$ m. (*b*) On the left is the small object with $l = 0.05$ m and on the right is the large object with $l = 0.35$ m.

particle image velocimetry) as these are very challenging to measure near the surface and around a moving object.

### 2.3. *Data acquisition*

Our goal is to examine the wave-induced drift of floating objects, investigate the effects of relative size and wave steepness, and understand the underlying mechanisms of drift enhancement by analysing the objects' oscillatory motions and local surface elevation amplitude distribution in their vicinity. To achieve this, we first measured the wave amplitude for each wave condition in the flume using the mean value obtained from all seven wave gauges. This measured wave amplitude is used to calculate wave steepness and, subsequently, the theoretical Stokes drift. Next, we extracted the objects' trajectories and the local surface elevation from the calibrated camera images. Image-processing techniques were used to calibrate the images, perform object tracking, and obtain the horizontal and vertical trajectories of the objects (only the horizontal trajectory for the small yellow balls). We used edge detection and curve line extraction methods to obtain the free surface elevation.

### 2.3.1. *Image processing and object tracking*

The small yellow balls were tracked using the CSRT algorithm in OpenCV in Python using images from Camera 2, allowing us to obtain their $(x, y)$-locations in pixel space. Care was taken to identify potential issues such as sphere collision and loss of tracking. The 2-D objects were tracked from the side of the flume using images from Camera 1. As the objects passed the vertical upright members of the wave flume structure, the camera's view of the objects was partially or entirely obscured depending on object size. This loss of sight meant that it was not possible to use the CSRT tracker for tracking objects from the side of the flume. Instead, the objects, which were painted yellow, were identified using an HSV mask in the HSV Colour space with OpenCV for each frame, followed by temporal advancement of the frame to get the time history of object motion. To remove background noise, unwanted stationary yellow elements were removed from the frame in a preliminary step. After applying the HSV mask, we extracted the contours of rectangular boxes with fixed sizes for each object. From these contours, we identified the position of the object's centre and calculated its roll angle in pixel space (we define the rotation of our objects around the $y$-axis as its roll motion). This method, in which we enforced that the tracked objects have a constant shape and size, meant it was possible to maintain tracking of the objects when they were partially obscured. Once the object trajectories were identified in pixel space, they were undistorted and transformed into physical space. The calibrated Camera 1 had an overall mean reprojection error of approximately 0.09 pixels (0.2 mm), while Camera 2 had a mean reprojection error of 0.46 pixels (0.6 mm). Examples of the horizontal trajectories are provided in figure 4(*a*).

### 2.3.2. *Edge detection to measure the free surface elevation*

It was not possible to operate wave gauges while the objects were in the flume, as they would obstruct the floating objects. To estimate the instantaneous free surface elevation while objects were in the flume, we used the images recorded by Camera 1. Surface elevation was extracted using edge-detection techniques. We set up virtual wave gauges that travelled with the objects, to obtain measurements of surface elevation a fixed positions relative to the objects. Specifically, we first determined the location of the objects for each frame and then established a group of virtual gauges with pre-set $x$-coordinates. The distance between the virtual gauges and the objects was kept constant. We set up 60 gauges with their relative position, $x - x_c$, ranging from $-1.1\lambda$ to $1.1\lambda$, in which $x$ represents the location of the wave gauges and $x_c$ the location of the centre of the object. To perform edge detection, we found that standard algorithms such as Canny edge detection and threshold approaches did not yield satisfactory results for our study. Therefore, we used the Holistically Nested Edge Detection (HED) algorithm, which employs a deep neural network capable of learning rich hierarchical edge maps (see Xie & Tu 2015 for more details). We used a pre-trained HED Caffe model to leverage the benefits of the HED algorithm (see Xie 2015). It is worth noting that while HED preserves boundaries in the image better than other methods, it produces more blurry boundaries than Canny edge detection. To enhance the sharpness of the edges, we applied the Zhang–Suen thinning algorithm using the 'ximgproc.thinning' function in OpenCV. By skeletonising the image, we obtained the surface elevation at the pre-set locations of the virtual wave gauges. Throughout the experiment, the positions of the objects and virtual wave gauges were

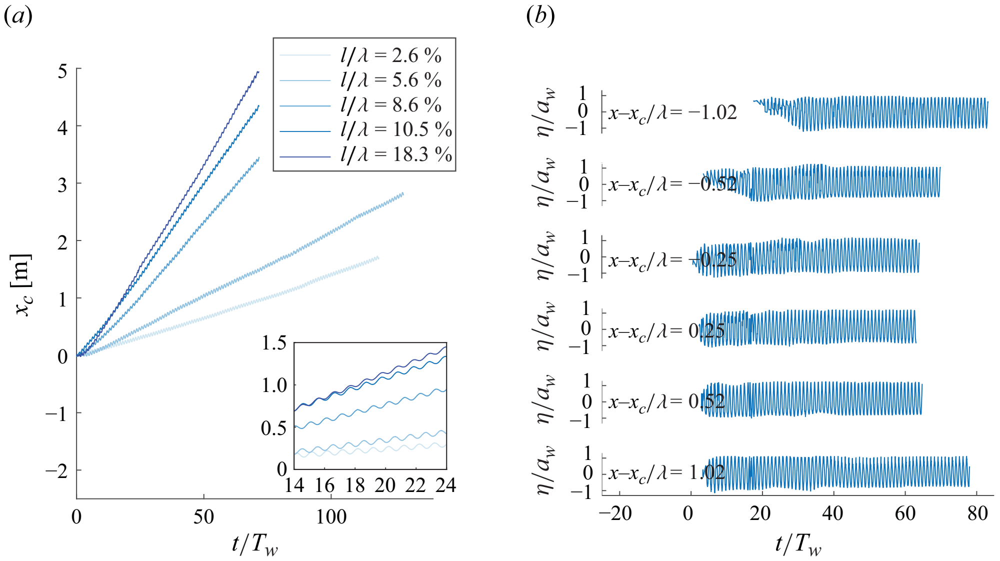

Figure 4. Example time history of objects' horizontal trajectories and surface elevation in regular waves with $f = 0.9$ Hz. (*a*) Horizontal trajectories of objects with different relative sizes for $ka_w = 0.10$, where $x_c$ is the horizontal position of the objects' centre, and $T_w$ denotes the wave period. (*b*) Local surface elevation of virtual gauges at various locations for $ka_w = 0.20$, where $x$ is the horizontal position of the virtual gauges, and $\eta$ is the local wave elevation. During the extraction process of the surface elevation for virtual wave gauges, the data are removed when the gauges are obscured by the flume's structural members or leave the pixel space (that is, when the position of the wave gauges is beyond the scope of the camera). Extraction begins when the object reaches $x_c = 2.3$ m and ends when it reaches $x_c = 8.2$ m, away from the wave maker.

updated with each frame as time progressed. Figure 4(*b*) provides examples of the time history of several virtual gauges, illustrating the variations in surface elevation.

### 2.3.3. *Data post-processing*

We aim to analyse the drift velocity, oscillatory linear motion in both the horizontal and vertical directions, as well as the magnitudes of local free surface elevations using the data obtained in §§ 2.3.1 and 2.3.2. The time-average drift and horizontal oscillatory motions are derived from the horizontal trajectories of the objects. Since it takes time for the object to accelerate and for its drift to reach a quasi-steady state, in which the drift speed is constant, we eliminate the initial transient from the data. The time required for an object to reach a quasi-steady state depends on its size and wave conditions. Generally, larger objects in larger waves take longer to reach a quasi-steady state due to their greater inertia and larger motion amplitudes. However, smaller objects move more slowly and are more sensitive to environmental disturbances such as lateral wave variations and friction. Consequently, there are some instances where we must wait longer for smaller objects to achieve a quasi-steady state before collecting data. Typically, the initial transient ranges from approximately 15 $T_w$ to 30 $T_w$ in duration, although in some cases, we wait up to 100 $T_w$ before commencing data collection. For small objects in low wave steepness, it may take over an hour for the object to reach the end of the flume, whereas for large objects in high wave steepness, this process can take as little as 35 s (in such cases, we conduct 2–3 repeats to ensure data over a sufficient number of wave periods). We analyse trajectories over durations ranging from approximately 450 $T_w$ to 1000 $T_w$ for smaller objects and 35 $T_w$ to 160 $T_w$ for large objects. Once the trajectory data are obtained, the horizontal motion is filtered by using low- and high-pass frequency filters to separate the sub-harmonic ($f/f_p \leq 0.4$) motion and linear motions ($0.4 < f/f_p \leq 1.7$), thus removing higher-order motion. The drift velocity is examined by performing a linear regression of the sub-harmonic motion with time. The amplitude of horizontal oscillatory motion (corresponding to the $x$-direction) is determined by performing zero-up-crossing analysis on the signal and calculating the mean magnitude over the full time duration. The analysis of vertical oscillatory motions and local wave amplitude distribution of the surface elevation follows a procedure similar to that of horizontal motions. Each trajectory and time history of the surface elevation undergoes a manual inspection as part of the quality-control process.

## 3. Existing theoretical and empirical models used for comparison

In this section, we outline the two models for drift enhancement (compared with the Stokes drift) that we will use to compare with our experimental results in § 4. The Stokes drift in finite water depth can be calculated by

$$u_S = c(a_w k)^2 \frac{\cosh\left(2k\left(d+z\right)\right)}{2\sinh^2\left(kd\right)}, \tag{3.1}$$

where $c = \omega/k$ is the wave celerity, $\omega = 2\pi f$ the angular frequency and $z$ the vertical coordinate of the fluid particle. For deep water ($kd \gg 1$), (3.1) becomes $u_S = c(a_w k)^2 e^{2kz}$. For the floating objects that we study, we evaluate the Stokes drift at $z = 0$. The only two models that we believe are suitable for comparison with our experimental results for large objects are the diffraction-modified Stokes drift model recently developed by Xiao *et al.* (2024) and the empirical formulas for drift enhancement proposed by Harms (1987). We will summarise the key equations of both models in turn.

### 3.1. *Diffraction-modified Stokes drift of Xiao et al. (2024)*

Xiao *et al.* (2024) showed that diffraction of the wave field affects wave-induced drift and cannot be neglected even for objects of $l/\lambda < 10\%$. They proposed a diffraction-modified Stokes drift akin to Stokes (1847) but considering the combination of the incident, diffracted and radiated wave fields. Here, we follow Xiao *et al.* (2024) and use a simplified boundary element method (BEM) model based on potential-flow theory to solve for the linear wave field. The total linear wave field is decomposed into its incident, diffracted, and radiated parts. If we describe the flow by a linear velocity potential $\varPhi$, it can be written as

$$\varPhi(x, z, t) = \varPhi_I(x, z, t) + \varPhi_D(x, z, t) + \varPhi_R(x, z, t), \tag{3.2}$$

where $\varPhi_I$, $\varPhi_D$ and $\varPhi_R$ are incident, diffraction and radiation potentials, respectively, then the diffraction-modified Stokes drift $u_{S,O}$ can be calculated by a second-order accurate expansion that is analogous to Stokes (1847), as shown by Xiao *et al.* (2024)

$$\begin{aligned} u_{S,O} &= \overline{\xi_x \frac{\partial^2 \varPhi}{\partial x^2} + \xi_z \frac{\partial^2 \varPhi}{\partial x \partial z}} \\ &= \overline{\xi_x \left( \frac{\partial^2 \varPhi_I}{\partial x^2} + \frac{\partial^2 \varPhi_R}{\partial x^2} + \frac{\partial^2 \varPhi_D}{\partial x^2} \right) + \xi_z \left( \frac{\partial^2 \varPhi_I}{\partial x \partial z} + \frac{\partial^2 \varPhi_R}{\partial x \partial z} + \frac{\partial^2 \varPhi_D}{\partial x \partial z} \right)}, \end{aligned} \tag{3.3}$$

where $\xi_x = \mathrm{Re}\{A_x e^{-\iota\omega t}\}$ and $\xi_z = \mathrm{Re}\{A_z e^{-\iota\omega t}\}$ are the linear horizontal and vertical harmonic oscillatory motions of the object, and the overline denotes averaging over a wave period. To evaluate (3.3), the linear oscillatory motions, the three potentials, and their derivatives are all calculated using a standard BEM model, as described in detail by Xiao *et al.* (2024).

Unlike the perturbation expansion in position applied by Stokes (1847) to an (infinitesimally small) Lagrangian particle to derive the Stokes drift, (3.3) is applied to an object of finite size. Equation (3.3) requires the evaluation of second derivatives of the velocity potential at a location where the velocity potential is not defined (i.e. at $\xi_x = \xi_x = 0$). Ideally, these second derivatives should be evaluated at the object's centre (of mass), which is outside of the domain where the potential-flow solutions apply (i.e. outside of the fluid domain). In practice, however, the second derivatives in (3.3) are determined based on the velocity potential evaluated at the object's boundaries, as described in Appendix A.5 of Xiao *et al.* (2024). For (3.3) to be a good approximation, the horizontal and vertical distances between the object's boundaries and its centre of mass need to be small. Formally, this requires the ratio of length of the object $l$ and the wavelength $\lambda$ to be small for the diffraction-modified Stokes drift model of Xiao *et al.* (2024) to apply, but not so small that the effects of diffraction themselves become insignificant.

### 3.2. *Empirical model of Harms (1987)*

In addition to the theoretical model of Xiao *et al.* (2024), we also compare the data with the empirical formulae proposed by Harms (1987) based on their extensive set of laboratory experiments for 2-D objects. According to Harms (1987), object drift can be estimated by

$$u_{S,O} = \begin{cases} 0.87\sqrt{gl}\,\dfrac{2a_w}{\lambda}\left(\dfrac{T_w}{T_{O,R}}\right)^{2.81+\log\frac{2a_w}{\lambda}} & \dfrac{T_w}{T_{O,R}} \leq 1.15, \\ 1.15\sqrt{gl}\,\dfrac{2a_w}{\lambda}\left(\dfrac{T_w}{T_{O,R}}\right)^{0.87+\log\frac{2a_w}{\lambda}} & \dfrac{T_w}{T_{O,R}} > 1.15, \end{cases} \tag{3.4}$$

where $T_w$ is the wave period and $T_{O,R}$ is the natural period of the roll motion of the object. Harms (1987) evaluated the natural period of the roll motion of the object $T_{O,R}$ in the slender-object limit ($l/h \gg 1$) and using empirical values of two coefficients obtained from the literature. This result is valid for the slender objects ($l/h > 3$) that Harms (1987) considered, whereas our objects all had an aspect ratio of $l/h = 1.5$. To estimate the natural roll period for each object, we conducted numerical simulations using the BEM model and identified the local peak value of the roll-mode response in waves of different frequencies. These responses were calculated for a range of frequencies from $f = 0.01$ to 4 Hz (corresponding to relative size $l/\lambda$ ranging from nearly 0 to 0.5, which covers the range of relative sizes considered in our study) with 0.01-Hz increments. We also identified the frequency corresponding to the peak value of the heave motion within this frequency range. For standard rectangular floating objects, the natural roll period can be estimated using (e.g. Baniela 2008)

$$T_{O,R} = 2\pi\sqrt{\frac{\rho h}{\rho_w g}\frac{(l^2+h^2)}{[l^2+6\rho/\rho_w(\rho/\rho_w-1)h^2]}} \tag{3.5}$$

where $\rho$ and $\rho_w$ denote the densities of the object and of water, respectively, and $g$ is the gravitational acceleration. We estimate the values of the natural roll and heave periods directly using the BEM. These periods, $T_{O,R,BEM}$ and $T_{O,H,BEM}$, and the roll period obtained from (3.5) are listed in table 5 for each object. From the table, it can be seen that the values of the roll period obtained from (3.5) ($T_{O,R}$) and from the BEM ($T_{O,R,BEM}$) agree closely.

| Object number | $T_{O,R,BEM}$ (s) | $T_{O,R}$ (s) | $T_{O,H,BEM}$ (s) |
|---|---|---|---|
| 1 | 0.61 | 0.55 | 0.40 |
| 2 | 0.88 | 0.78 | 0.56 |
| 3 | 1.08 | 0.99 | 0.72 |
| 4 | 1.15 | 1.08 | 0.81 |
| 5 | 1.67 | 1.53 | 1.05 |

Table 5. Estimated natural periods of object heave and roll motion. Object numbers 1–5 correspond to the objects specified in table 3. The periods $T_{O,R,BEM}$ and $T_{O,H,BEM}$ are the estimated natural periods of roll and heave motions for the objects calculated from the BEM simulations. The natural roll period $T_{O,R}$ can be obtained directly using (3.5).

| $l/\lambda$ (%) | 2.6 | 5.2 | 8.4 | 10.5 | 12.5 | 15.6 | 18.3 | 22.4 | 24.8 | 27.1 |
|---|---|---|---|---|---|---|---|---|---|---|
| Object number | 1 | 2 | 3 | 4 | 3 | 4 | 5 | 5 | 5 | 5 |
| $T_w$ (s) | 1.11 | 1.11 | 1.11 | 1.11 | 0.91 | 0.91 | 1.11 | 1.00 | 0.95 | 0.91 |
| $T_w/T_{O,R,BEM}$ | 1.83 | 1.27 | 1.03 | 0.97 | 0.85 | 0.79 | 0.67 | 0.60 | 0.57 | 0.55 |
| $T_w/T_{O,H,BEM}$ | 2.74 | 1.97 | 1.54 | 1.37 | 1.26 | 1.12 | 1.06 | 0.95 | 0.90 | 0.86 |

Table 6. Estimates of the ratio of natural heave and roll period for objects with different relative sizes to incident wave periods (see table 4 for object dimensions and table 5 for values of the natural period).

To further validate our approach to calculating the roll period, we compared our estimate with the value obtained for a floating cuboid in the study by He *et al.* (2016). The cuboid in their study had dimensions $b = 0.42$ m, $l = 0.3$ m, $h = 0.2$ m, and $h_d = 0.1$ m, with a density of $\rho = 500\,\mathrm{kg\,m^{-3}}$. For this geometry, our estimate of the roll period is $T_{O,R,BEM} = 1.85$ s and the period derived from the experiments of He *et al.* (2016) is 1.6 s. We note that the free-damped oscillation decay test used by He *et al.* (2016) will be affected by viscosity, whereas our (potential-flow) estimate only accounts for radiation damping. Nevertheless, we can conclude that our BEM-based estimates provide reasonable estimates of the natural roll period. We note that the empirical parametrisation (3.4) suggests that the drift peaks when $T_w/T_{O,R} = 1.15$. Values of $T_w/T_{O,R}$ we use for all of the objects considered in our study, alongside values of $T_w/T_{O,H}$, are listed in table 6.

## 4. Results and analysis

In this section, we present the results of our laboratory experiments, focusing on the linear oscillatory motion, drift velocities, and the local wave amplitude distributions of the wave field surrounding the objects. We compare the results of our laboratory experiment with the models in § 3 and analyse the effects of object size and wave steepness in turn. Before analysing our results for drift, we must take into account the Eulerian-mean background current. Appendix B provides a comprehensive assessment of the repeatability of our experiments.

### 4.1. *Eulerian-mean background current*

After estimating the Lagrangian-mean drift of objects $\overline{u}_{L,O}$ based on the data acquired in § 2.3, we can calculate what we define as the ‘Stokes object drift’ $u_{S,O}$. The Stokes object drift is defined analogously to the Stokes drift (cf. Bühler 2014) as $u_{S,O} \equiv \overline{u}_{L,O} - \overline{u}_E$, in which $\overline{u}_E$ is the Eulerian-mean velocity. In flumes, $\overline{u}_E$ usually takes the form of a

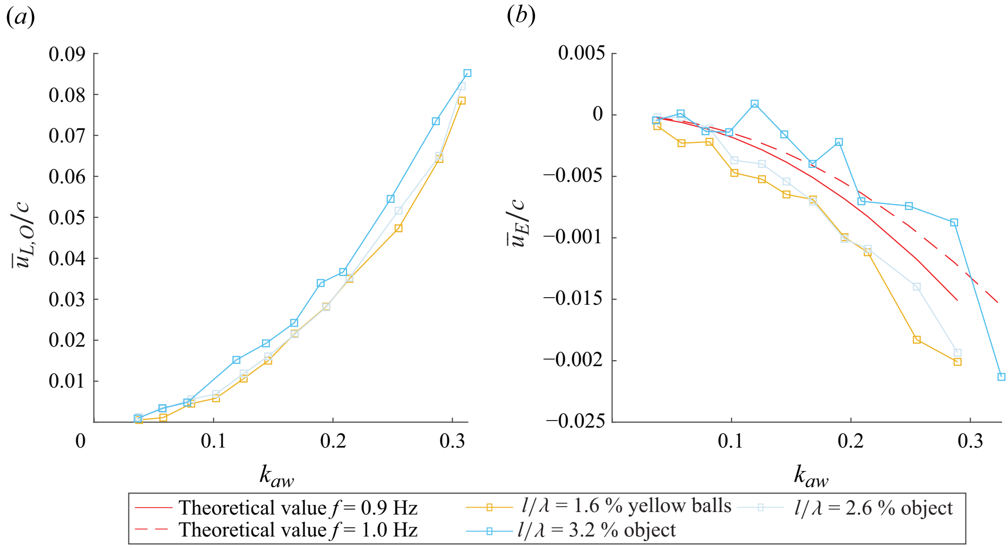

Figure 5. Lagrangian drift of small objects and the Eulerian-mean velocity on the surface as a function of wave steepness in waves with frequencies of $f = 0.9$ Hz and $f = 1.0$ Hz. (*a*) Lagrangian drift, normalised by wave celerity $c$ where $c = \omega/k$ is the ratio of angular frequency to wave number, of the 3-D small yellow balls ($l = D = 0.02$ m) with $l/\lambda = 1.6\%$ and the smallest 2-D objects with $l/\lambda = 2.6\%$ and $l/\lambda = 3.2\%$. (*b*) Comparison of wave-celerity normalised Eulerian-mean velocity derived from experiments and theory (4.1). The values of $\overline{u}_E$ for $l/\lambda = 2.6\%$ and $l/\lambda = 1.6\%$ are obtained by $\overline{u}_E = \overline{u}_{L,O} - u_{O,S} = \overline{u}_{L,O} - u_S$, in which $\overline{u}_{L,O}$ is the Lagrangian drift of the corresponding objects that is directly measured in the wave flume and $u_S$ is the theoretical Stokes drift (3.1), which is equal to the Stokes object drift for such small objects.

return current. We note that the appearance of the Eulerian-mean current (at the front of the wave train, i.e. from the beginning of wave generation) does not entail a temporal delay. The first arrival of waves from the wave maker is like the first half of a wave group, and a group-like structure immediately experiences divergent Stokes transport and induces the Eulerian-mean return flow (e.g. Van Den Bremer & Taylor 2015; Van den Bremer & Taylor 2016). The factors dependent on time (that are thus not instantaneous) are the development, transport and diffusion of vorticity, which subsequently alter the Eulerian current in a complex way (Longuet-Higgins 1953; Van den Bremer & Breivik 2018). To examine the Eulerian-mean velocity in our flume, we use small ($D = 0.02$ m), yellow, spherical 3-D balls with a density close to that of water ($\rho_p = 920\,\mathrm{kg\,m^{-3}}$) as current drogues, which are expected to behave as accurate Lagrangian tracers based on their size and density (cf. Nath 1978; Harms 1987; Alsina *et al.* 2020; Eeltink *et al.* 2023). As the drift behaviour of 3-D balls is assumed to be purely Lagrangian, they are transported at the speed of the Stokes drift when the Eulerian-mean velocity is removed (i.e. $u_{S,O} \equiv \overline{u}_{L,O} - \overline{u}_E = u_S$ when $\overline{u}_E = 0$). For equivalent wave conditions and similar time durations in the same tank, we assume the Eulerian-mean flows at the surface for all objects are equal. Figure 5(*a*) shows the Lagrangian drift $u_{L,O}$ of the small yellow balls and of the smallest 2-D object ($l = 0.05$ m) as a function of wave steepness. The Lagrangian drifts of the balls, which are 3-D, and the small 2-D objects are found to be similar, indicating that the 2-D objects with a relative size of $l/\lambda = 2.6\%$ exhibit predominantly Lagrangian drift behaviour and are transported at a speed equal to the Stokes drift when the Eulerian-mean velocity is removed. We also compare the measured Eulerian-mean drift obtained from the experiments with theoretical values in figure 5(*b*). The volume flux induced by the Stokes drift is equal to $Q_S = \int_{-d}^{0} u_S(z)\mathrm{d}z$; the volume flux associated with the Eulerian-mean return current is $Q_E = \int_{-d}^{0} u_E(z)\mathrm{d}z$. By assuming the Eulerian-mean return current $\overline{u}_E$ is depth uniform (i.e., it has zero vorticity) and by balancing the volume fluxes (i.e. $Q_S + Q_E = 0$), we obtain $\overline{u}_E = -Q_S/d$ and thus

$$\overline{u}_E = -\frac{\int_{-d}^{0} u_S(z)\mathrm{d}z}{d} = -\frac{1}{d}\int_{-d}^{0} \frac{c(a_w k)^2 \cosh 2k(d+z)}{2\sinh^2(kd)}\mathrm{d}z, \tag{4.1}$$

where $d$ is the water depth, $u_S(z)$ is the vertical distribution of Stokes drift, $c$ the wave celerity, $k$ the wavenumber and $a_w$ the wave amplitude. Surprisingly (see Van den Bremer & Breivik (2018) and Monismith (2020) for context), the Eulerian-mean velocity in the flume appears to be predicted very well by (4.1) (for an incident wave frequency with $f = 0.9$ Hz). It is well known that analytical estimates and experimental measurements of the return current for regular waves are sensitive to the exact assumptions used and the boundary conditions within a given flume and that predicted and measured values often differ (Van den Bremer & Breivik 2018). Nevertheless, our observations indicate that the theoretically estimated Eulerian-mean flow agrees with calculations derived from the reference experiments with yellow balls.

Given this good agreement, we use the theoretical values of Eulerian-mean velocity (4.1) to evaluate the Stokes object drift $u_{S,O}$ from the measured Lagrangian-mean object drift $\overline{u}_{L,O}$ for all objects. The expression for the Stokes object drift is then given by

$$u_{S,O} = \overline{u}_{L,O} - \overline{u}_E = \overline{u}_{L,O} + \frac{1}{d}\int_{-d}^{0} \frac{c(a_w k)^2 \cosh 2k(d+z)}{2\sinh^2(kd)}\mathrm{d}z. \tag{4.2}$$

### 4.2. *Effect of object size and wave steepness*

To examine the effects of relative object size and wave steepness, we will first look at the oscillatory motion and then the Stokes object drift followed by the local wave amplitude distribution. The linear oscillatory motions in both the horizontal and vertical directions are given in figure 6 as a function of wave steepness, and in figure 7 as a function of relative size. The motions are normalised by the corresponding wave amplitudes $a_w$ measured using wave gauges in the wave flume without objects. The Stokes object drift obtained using (4.2) is reported in figure 8 as a function of wave steepness and relative size. For clarity, we do not plot all the measured data in each figure (that is, we do not present the data for $l/\lambda = 12.5\%$, 15.6%, 22.4% and 24.8% in figure 8(*a*), but include these data in figure 8(*b*). By time averaging the time history of the local surface elevations of all moving virtual wave gauges (as described in § 2.3), we obtain the local wave amplitude distribution $a(x)$ as a function of the relative distance between the gauges and the object's centre. Figure 9 plots the normalised local wave amplitude distribution $a(x)/a_w$ for objects of different relative sizes when $ka_w = 0.21$ and figure 10 plots this distribution for an object of $l/\lambda = 18.3\%$ for different values of wave steepness.

#### 4.2.1. *Oscillatory motion*

We start by looking at the horizontal oscillatory motion. As shown in figure 6(*a*) and figure 7(*a*), when the objects are small, with a relative size of $l/\lambda \lesssim 5\%$, the magnitude of the horizontal motions is very close to the incident wave amplitude $a_w$, implying behaviour is essentially Lagrangian. The amplitude of horizontal motion decreases at an approximately linear rate as the relative object size increases. This trend applies to all objects in the size range we considered and is independent of wave steepness. For fixed relative size, the non-dimensional motion does not vary significantly with wave steepness ($ka_w \lesssim 0.25$). For the highest wave steepness, $ka_w = 0.31$, the non-dimensional horizontal

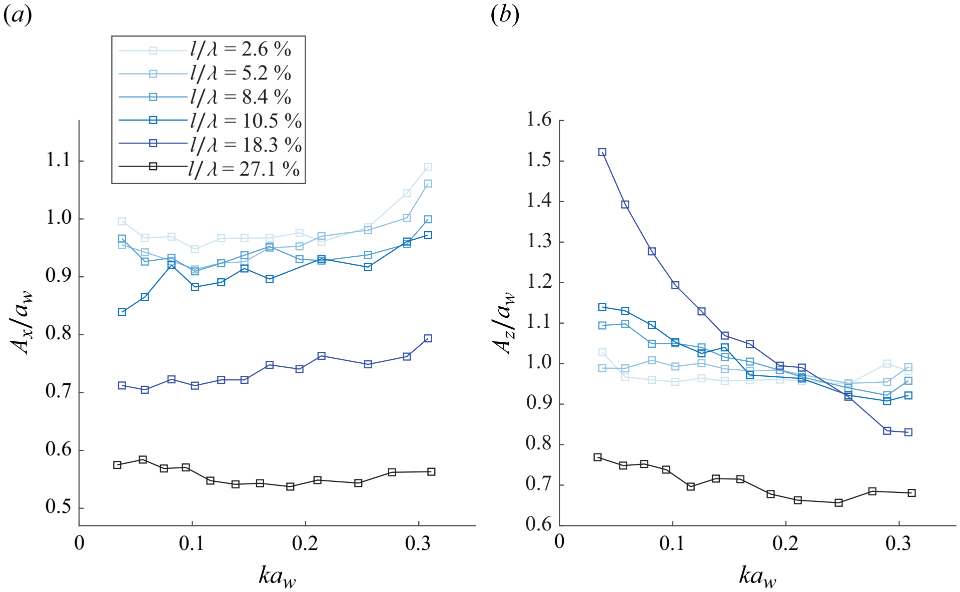

Figure 6. Linear oscillatory motion amplitudes as a function of wave steepness for objects of different relative size. (*a*) Magnitude of horizontal motion normalised by wave amplitude. (*b*) Magnitude of vertical motion normalised by wave amplitude.

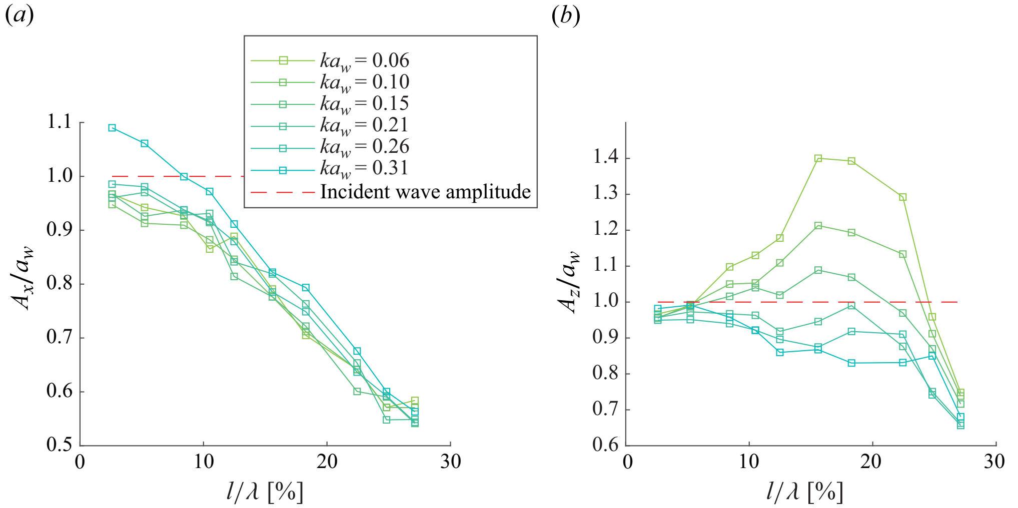

Figure 7. Linear oscillatory motion amplitudes as a function of the relative size of the objects for different wave steepness. (*a*) Magnitude of horizontal motion normalised by wave amplitude. (*b*) Magnitude of vertical motion normalised by wave amplitude.

motion is slightly larger than for lower values of wave steepness, and this difference is greatest for smaller objects $l/\lambda \lesssim 15.6\%$. This could be a nonlinear phenomenon for which we cannot account for, but may also arise because smaller objects are more sensitive to imperfections of the wave field in the flume due to their lower inertia. As waves become very steep (near the limits of the wavemaker), both wave reflection and lateral variations

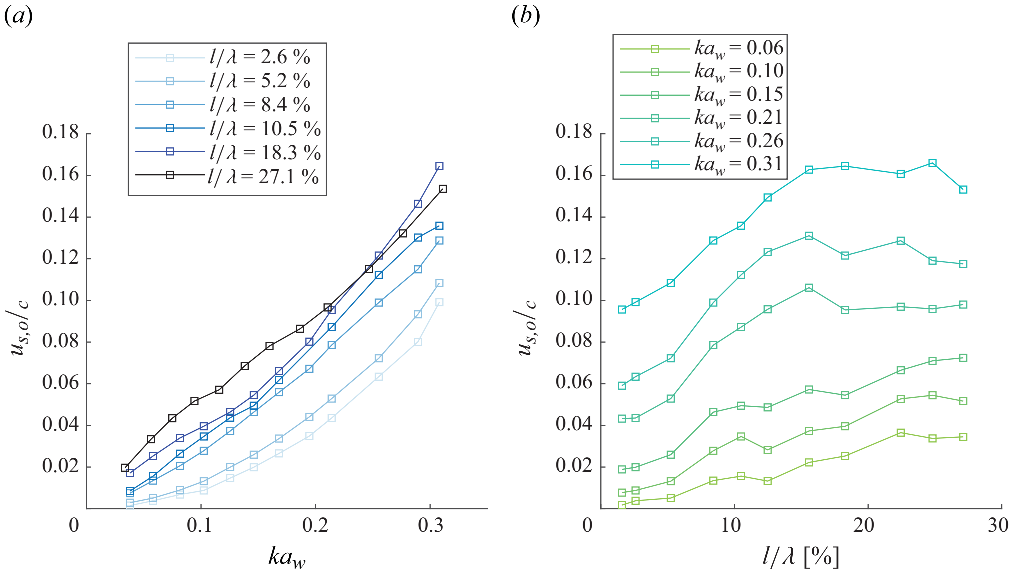

Figure 8. Celerity-normalised Stokes object drift velocity (*a*) as a function of wave steepness for different relative object sizes and (*b*) as a function of relative size for different wave steepness.

in the wave field deteriorate, affecting both the value of the incident wave amplitude $a_w$ (used for normalisation) and the motion response of the objects.

The vertical motion of the objects exhibits a more complex behaviour, as shown in figures 6(*b*) and 7(*b*). When the objects are very small, they behave like Lagrangian particles. However, as the object size increases, the non-dimensional vertical motion becomes dependent on both wave steepness and relative object size. Considering the dependence on relative size first, at low wave steepness, $ka_w \lesssim 0.15$, the vertical motion increases with relative object size when $l/\lambda \lesssim 15.6\%$, but decreases with size when $l/\lambda \gtrsim 18.3\%$. At high wave steepness, $ka_w \gtrsim 0.20$, the vertical motion always decreases with relative size, with a more pronounced decrease for larger objects, $l/\lambda \gtrsim 22.4\%$. The behaviour of vertical motion as a function of wave steepness also varies depending on the object size. When the object is either very small, $l/\lambda \lesssim 5.2\%$ or very large, $l/\lambda = 27.2\%$, its non-dimensional vertical motion remains independent of wave steepness. However, for objects with intermediate sizes with $8.4\% \lesssim l/\lambda \lesssim 24.8\%$, their non-dimensional vertical motion decreases with increasing wave steepness. This decreasing trend is most pronounced for objects with a relative size of $l/\lambda = 15.6\%$, 18.3% and 22.4%. We believe that this behaviour may be attributed to the effect of a resonance in the vertical direction, although we do not fully explain it here.

### 4.2.2. *Stokes object drift*

The Stokes object drift, normalised by wave celerity, shown in figures 8(*a*) and 8(*b*), exhibits a clear dependence on both object size and wave steepness. In general, for low wave steepness, $ka_w \lesssim 0.15$, the Stokes object drift increases with relative size for all the object sizes covered here (i.e., $2.6\% \leq l/\lambda \leq 27.2\%$). However, for relatively high wave steepness, $ka_w \gtrsim 0.17$, the drift shows a different trend. It increases with object size for $l/\lambda \lesssim 15.6$ but exhibits a decreasing trend for $l/\lambda \gtrsim 15.6$. Changes in the functional dependence of the Stokes object drift on the wave steepness are also evident. Drift always increases with increasing wave steepness. For small objects (i.e. $l/\lambda = 2.6\%$), this increase

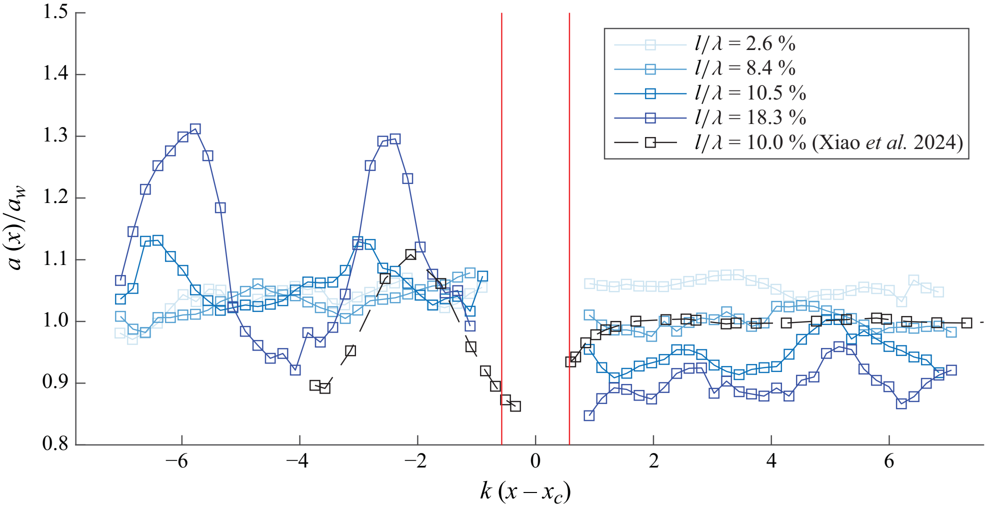

Figure 9. Non-dimensional local surface elevation amplitude distribution, $a(x)/a_w$, as a function of horizontal distance (scaled by wavenumber) from the centre of mass of the object, $k(x - x_c)$, for objects of different relative sizes with incident wave steepness $ka_w = 0.21$, and frequency $f = 0.9$ Hz. The black dashed line denote the results from the numerical model of Xiao *et al.* (2024) for $l/\lambda = 10\%$, where the incident wave steepness is $ka_w = 0.034$ and the wave frequency is $f = 0.65$ Hz. The red lines represent the left and right sides of the largest object with a relative size of $l/\lambda = 18.3\%$.

appears to be quadratic, whereas for larger objects, the relationship between drift and steepness appears to be closer to linear – we will consider this in more detail in § 4.3 (see also Tanizawa *et al.* (2001) and He *et al.* (2016) for similar observations). The relative size at which this transition in both the vertical motion and the drift behaviour occurs lies in the range $T_w/T_{O,H} = [1.07, 1.31]$ (or $T_w/T_{O,R} = [0.6, 0.84]$). In contrast to the suggestion by Harms (1987) that the drift reaches a maximum at $T_w/T_{O,R} = 1.15$ (cf. (3.4)), our observations suggest that for objects with small aspect ratio, for which relative size the maximum (peak) values in vertical motions and drift rates occur, depends on $T_w/T_{O,H}$ (e.g. the peak value of the drift occurs when the ratio is equal to 1.15).

### 4.2.3. *Local wave amplitude distribution*

Next, we examine the wave field in the vicinity of the object. Specifically, we examine the wave amplitude distribution at virtual probes that are stationary in the reference frame of the object (the reference frame drifts and oscillates horizontally with the object). In this reference frame, the amplitude field has a spatial distribution (consisting of nodes and antinodes), which is obtained by time averaging the amplitudes at each virtual probe location (in the reference frame of the object) over time after reaching a quasi-steady state. The local wave amplitude distribution in the vicinity of the moving object thus obtained is shown in figure 9. Note that we have corrected the wave elevation obtained from edge detection to address potential measurement errors in the camera data. This correction is achieved by using reference data of wave elevation in the absence of the object and ensuring consistency of this data with the wave gauge data collected in the tank (i.e. $a_w$), which is used for normalisation.

Figure 9 also shows the results from the numerical simulations of Xiao *et al.* (2024). There are two important differences between the surface amplitude distribution obtained from experiments in the present paper and from numerical simulations of Xiao *et al.* (2024) that only make a qualitative comparison between the two possible. First, the results

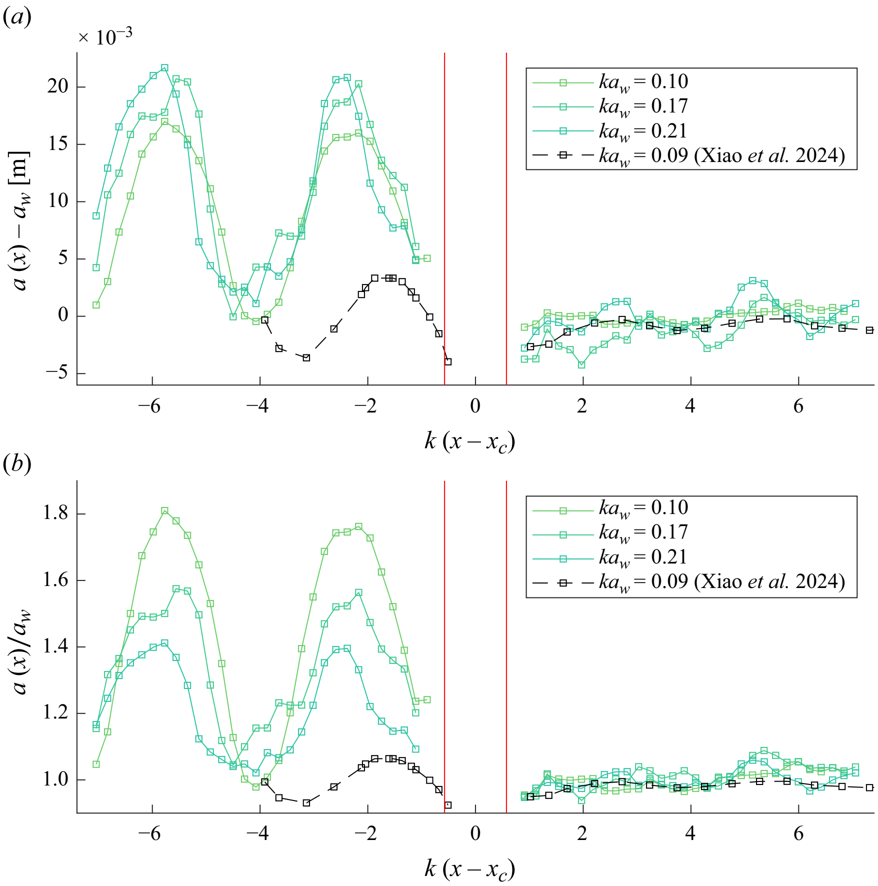

Figure 10. Local surface elevation amplitude distribution, $a(x)$, as a function of horizontal distance (scaled by wavenumber) from the centre of mass, $k(x - x_c)$, for the largest object with a relative size of $l/\lambda = 18.3\%$ at a frequency of $f = 0.9$ Hz. (*a*) Difference between the local surface elevation amplitude and the incident wave amplitude, $a(x) - a_w$, for three different wave steepnesses. (*b*) Ratio of local surface elevation and incident wave amplitudes, $a(x)/a_w$, for three different wave steepnesses. The black dashed lines denote the results from the numerical model of Xiao *et al.* (2024) for $l/\lambda = 10\%$ with incident wave steepness $ka_w = 0.09$ and wave frequency $f = 0.65$ Hz. The red lines represent the left and right sides of the object.

from Xiao *et al.* (2024) are for lower wave steepness ($ka_w = 0.034$). When the wave steepness becomes too high, the large drift of the object causes large mesh deformation, making the dynamic mesh-based numerical model less accurate. This challenge does not arise in our experiments, where it is, in fact, easier to measure the surface amplitude distribution for higher steepness. The second difference is the reference frame in which the surface amplitude distributions are obtained. Xiao *et al.* (2024) used ‘gauges’ to output the surface elevation that were fixed in the stationary reference frame. In Xiao *et al.* (2024), implementing moving gauges was shown to be prohibitively computationally expensive, as the gauges move with the object horizontally every time step. The reason Xiao *et al.* (2024) could still observe a standing wave pattern in the stationary reference frame is probably due to the relatively small magnitude of the drift therein.

It is clear from figure 9 that a standing wave pattern forms that is clearest for relatively large objects, $l/\lambda =$ 10.5% and 18.3%. The local amplitude of the surface elevation is normalised by the wave amplitude in the absence of the object, $a_w$. Similar to observations by Xiao *et al.* (2024), for small objects, $l/\lambda = 2.6~\%$, the local time-averaged wave amplitude does not vary significantly with distance to the object's centre. It remains relatively constant at a value of $a(x)/a_w = 1.0$, suggesting negligible disturbance to the wave field and no standing waves. As the object size increases, a standing wave pattern becomes apparent. On the upstream side, the time-averaged wave amplitudes show a pattern of smaller and larger amplitudes compared with the incident wave field (or compared with the case of a very small object) at different distances from the object's centre. The standing wave pattern thus identified is more evident as the object becomes larger. On the downstream side, (somewhat) smaller amplitudes are observed for all locations, and there is a discernible difference in the magnitude of the surface elevation between the two sides of the object for large enough objects. The formation of the standing wave pattern is explained by Xiao *et al.* (2024) using their numerical model. As the object is large enough to diffract the wave field, it 'disrupts' the wave field and 'impedes' the passage of waves, leading to local blocking. This disturbance results in a difference between wave amplitudes on the upstream and downstream sides of the object. We note that, as described in § 2.3.2, the locations of the virtual wave probes are continuously updated in time to maintain a constant horizontal distance relative to the object's centre. Consequently, the standing wave pattern observed only occurs in the reference frame of (and thus stationary relative to) the object.

In figure 10, we show how the standing wave pattern varies with steepness for relatively large objects (large enough to generate a clear standing wave pattern). The standing wave pattern is plotted as $a(x) - a_w$ in figure 10(*a*) and as $a(x)/a_w$ in figure 10(*b*), for an object of size $l/\lambda = 18.3\%$. The pattern is clearer when plotted as an absolute value (that is, as $a(x) - a_w$) as incident wave steepness increases from $ka_w = 0.10$ to $ka_w = 0.21$, while the pattern is less evident when plotted as a normalised value (that is, as $a(x)/a_w$) as steepness increases. This observation aligns with previous findings of Xiao *et al.* (2024), as increasing wave steepness increases the wave-celerity normalised Stokes object drift, while decreasing the Stokes-drift-normalised Stokes object drift. If we consider two identical waves with an angular frequency of $\omega$, wavenumber $k$ and wave amplitude $a_w$, propagating in opposite directions (i.e. 100 % reflection by the object), the resultant wave elevation $\eta(x, t)$ would take the form $\eta(x, t) = 2a_w \sin(kx) \cos(\omega t)$. By taking the modulus of the wave amplitude distribution ($|2 \sin(kx)|$), we obtain the standing wavelength, which is half that of the incident waves. Indeed, the wavelength of the standing wave pattern depicted in figures 9 and 10 is $\lambda_{sw} = 1.05$ m, approximately half of the incident wavelength $\lambda = 1.91$ m. We note that the effect of evanescent waves may be included in the estimate of $\lambda_{sw}$, as well as the effects of phase differences that result from the distance to the wave probe being measured relative to the object's centre of mass, rather than its boundaries (the horizontal positions of the boundaries relative to the (virtual) probe change constantly as the object moves and rotates). Moreover, the (virtual) wave probes are set with a certain spatial resolution, which may introduce small errors in determining maxima and minima and their exact locations, from which $\lambda_{sw}$ is estimated.

Despite obvious general qualitative agreement, there are two ways the standing wave pattern found here is different from that identified by Xiao *et al.* (2024), as shown in figures 9 and 10: (1) the phase difference between the standing wave patterns formed by objects of different sizes and (2) the sign of the difference in amplitude between the two sides of the object. First, Xiao *et al.* (2024) found that the local maxima and minima in the amplitude distribution occurred at similar relative distances for objects of different sizes, which is not the case here (cf. Figure 9). Second, in Xiao *et al.* (2024), the local surface elevation amplitude on the upstream side of the object (i.e., the locations just to the left of the leftmost vertical red line in figure 9) is smaller than on the downstream side

| | $p_{00}[\times 10^{-2}]$ | $p_{10}[\times 10^{-2}]$ | $p_{01}$ | $p_{20}[\times 10^{-2}]$ | $p_{11}[\times 10^{-2}]$ | $p_{02}$ | $R^2$ |
|---|---|---|---|---|---|---|---|
| All terms retained | $-3.10\pm0.40$ | $0.46\pm0.04$ | $0.14\pm0.04$ | $-0.01\pm0.00$ | $0.40\pm0.09$ | $0.80\pm0.09$ | 0.98 |
| $p_{00}=0$ | — | $0.26\pm0.03$ | $-0.07\pm0.03$ | $-0.00\pm0.00$ | $0.79\pm0.09$ | $1.19\pm0.10$ | 0.97 |
| $p_{00}=0,\ p_{20}=0$ | — | $0.08\pm0.02$ | $0.03\pm0.03$ | — | $0.60\pm0.10$ | $1.00\pm0.10$ | 0.96 |

Table 7. Coefficients of the regression of wave-celerity normalised Stokes object drift $u_{S,O}/c$ on wave steepness $\epsilon = ka_w$ given by (4.3). The error bounds represent ± one standard deviation of the coefficients, and $R^2$ is the coefficient of determination.

(i.e. the location just to the right of the rightmost vertical red line in figure 9), while our experiment shows the opposite. The discrepancies are likely due to our (virtual) gauges moving with the objects (i.e. the distance between the gauges and the object is constant), while the gauges in Xiao *et al.* (2024) were fixed in a stationary reference frame, causing a phase shift and a non-stationary standing wave pattern.

### 4.3. *A new empirical parametrisation for enhanced Stokes object drift*

To quantitatively describe the effects of relative size $l/\lambda$ and wave steepness $\epsilon = ka_w$ in our experimental observations, we perform the following polynomial regression for the wave celerity-normalised Stokes object drift $u_{S,O}/c$

$$u_{S,O}/c = p_{00} + p_{10}\left(\frac{l}{\lambda}\right) + p_{01}\epsilon + p_{20}\left(\frac{l}{\lambda}\right)^2 + p_{11}\left(\frac{l}{\lambda}\right)\epsilon + p_{02}\epsilon^2, \tag{4.3}$$

where $p_{00}$, $p_{10}$, $p_{01}$, $p_{11}$ and $p_{02}$ are the coefficients to be determined. We have chosen a second-order bi-variate polynomial functional form in (4.3) for its simplicity and because previous experimental studies have revealed a mixture of linear and quadratic correlations between drift, object size and steepness (Harms 1987; Tanizawa *et al.* 2001; Huang & Law 2013) (as discussed in § 1.4). We note that idealised Lagrangian particles have a (celerity-normalised) drift, the Stokes drift (3.1), that is (only) quadratic in steepness. We consider cases with all terms retained as well as those with several terms set to zero. Table 7 shows the coefficient values obtained from the regression with 95% confidence bounds. To ensure independence between the covariates, which were varied independently in our experimental matrix, we have also estimated the population Pearson correlation between relative size $l/\lambda$ and wave steepness $\epsilon$, finding a very small sample correlation coefficient $O(10^{-18})$. There is clear evidence that the Stokes object drift is dependent on both linear and quadratic terms in wave steepness ($\epsilon$ and $\epsilon^2$); the coefficient on the quadratic term is the most significant followed by the linear term. Ideally, if both the wave steepness and relative size of the object are 0, the drift should be zero, so we set $p_{00} = 0$. The fact that this (setting $p_{00} = 0$) significantly changes the regression coefficients suggests that the simplified combination of linear and a quadratic terms has limitations. The quadratic term in $l/\lambda$ is insignificant, and we set it to zero ($p_{02} = 0$). We thus propose the simplified relationship

$$u_{S,O}/c = 0.0008\left(\frac{l}{\lambda}\right) + 0.03\epsilon + 0.0060\left(\frac{l}{\lambda}\right)\epsilon + 1.0\epsilon^2. \tag{4.4}$$

This simplified model provides a reasonably accurate representation of the wave celerity-normalised Stokes object drift in terms of relative size and wave steepness, with the most significant contributions coming from the linear and quadratic terms of wave steepness.

However, it is important to note that this simplified model is specific to the experimental data and may not capture all possible complexities of the drift behaviour. We have also conducted a similar polynomial regression of drift normalised by Stokes drift as a function of relative size and wave steepness. However, the results suggest that higher-order terms (at least a third order) of wave steepness need to be considered to make $R^2$ larger than 0.9, indicating potentially complex behaviour that goes beyond a simple polynomial model.

### 4.4. *Comparison with existing theoretical and empirical models*

In this section, we set out to assess the range, in terms of relative object size and wave steepness, over which the classical Stokes drift (given by (3.1)), the diffraction-modified Stokes drift of Xiao *et al.* (2024) (given by (3.3)) and the empirical formulae of Harms (1987) (given by (3.4)) are valid. This has been done by comparing the drifts from experimental measurement to those predicted by three different models and by examining their effectiveness in a parameter space made up from two parameters: relative size and wave steepness. To facilitate the comparison, we use two different normalisation techniques for the drift: celerity normalisation and Stokes-drift normalisation, and then examine the normalised drift as a function of relative object size and wave steepness. We first compare the experimental measurements to the theoretical Stokes drift and the diffraction-modified Stokes drift model of Xiao *et al.* (2024) by normalising the drift by the theoretical Stokes drift and showing this as a function of relative object size and wave steepness, respectively. Next, a comparison is drawn between the experimental results and the empirical formula by (3.4), along with the diffraction-modified Stokes drift, as a function of relative size for different values of wave steepness. To help explain any discrepancies between measurements and model predictions, the amplitude of the linear oscillatory motion values derived from experiments are compared with those predicted by the BEM model, which is used to calculate the diffraction-modified Stokes drift in (3.3).

The experimentally measured Stokes object drift scaled by the theoretical Stokes drift as a function of wave steepness and relative object size are presented in figures 11(*a*) and 11(*b*), respectively. As shown in panel (a), small objects $l/\lambda \leq 2.6\%$ follow the theoretical Stokes drift. As the object size increases, the amplification factor $u_{S,O}/u_S$ increases, suggesting a larger drift enhancement. This is true for all values of wave steepness but is especially evident for smaller values of wave steepness. For objects of a certain size, the amplification factor decreases drastically as wave steepness increases in the low to intermediate wave steepness range, reaching its peak value at the lowest wave steepness. As the wave steepness increases further, the amplification factor either becomes constant or decreases slowly with steepness. A decreasing trend with wave steepness is more distinct for larger objects and was also observed in measurements by Huang *et al.* (2011), although they do not explicitly discuss this.

Comparison between the experimentally measured Stokes object drift and the diffraction-modified Stokes drift normalised by theoretical Stokes drift is made in figure 11(*b*). In addition, a comparison between the measured Stokes object drift, the diffraction-modified Stokes drift proposed by Xiao *et al.* (2024) and the empirical formula of Harms (1987) is made in figure 12 by examining the drift normalised by wave celerity $c$ as a function of relative size for different values of wave steepness. The figures show that for small objects, the diffraction-modified Stokes drift accurately predicts Stokes object drift for various values of steepness, but this agreement breaks down for relatively large objects, for which the expansion that underlies (3.3) is no longer valid. As shown in both figures 11(*b*) and 12, the diffraction-modified Stokes drift is capable of giving a good prediction beyond the range of the classical Stokes drift.

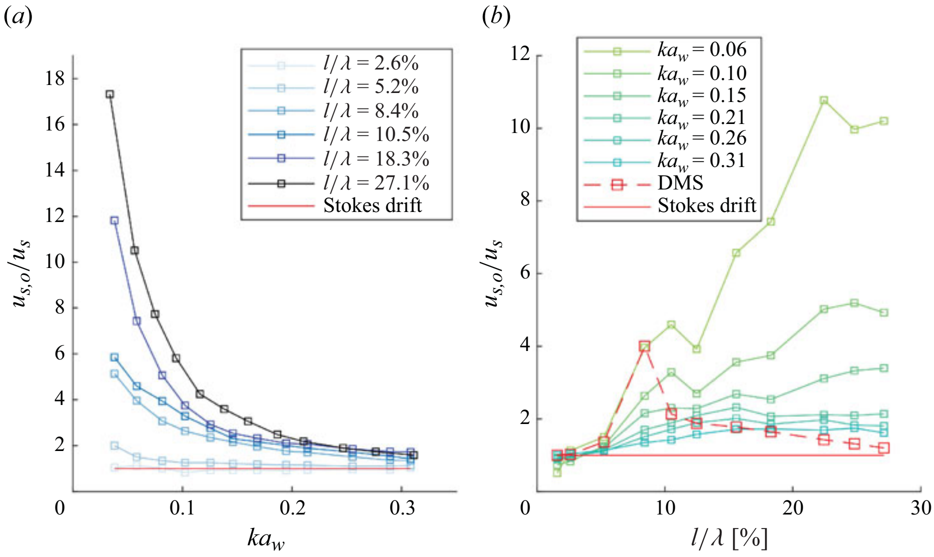

Figure 11. Stokes drift-normalised Stokes object drift (*a*) as a function of wave steepness for different relative object sizes and (*b*) as a function of relative size for different values of wave steepness. An idealised Lagrangian particle with zero enhanced drift would have $u_{S,O}/u_S = 1$. The red dashed line with red square labelled DMS represents the diffraction-modified Stokes drift given by (3.3). As the diffraction-modified Stokes drift for a certain object size does not change with wave steepness (we use a linear 'BEM' model to solve (3.3), and (3.3) is a second-order accurate quantity), it is shown as a single line in panel (*b*).

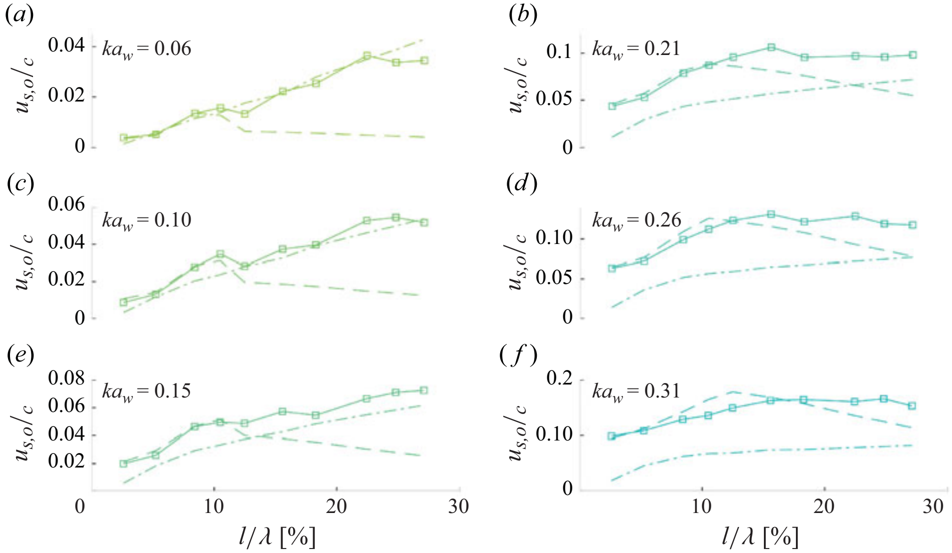

Figure 12. Comparison of the Stokes object drift from experiments with the diffraction-modified Stokes drift (3.3) proposed by Xiao *et al.* (2024) and the empirical formula (3.4) of Harms (1987) as a function of relative object size for different values of wave steepness. The drift is normalised by wave celerity. Markers connected by continuous lines correspond to the results from experiments, dashed lines (of the same colour, corresponding to the colour in figure 11(*b*) to the diffraction-modified Stokes drift, and dash-dotted lines (of the same colour) to the empirical formula of Harms (1987).

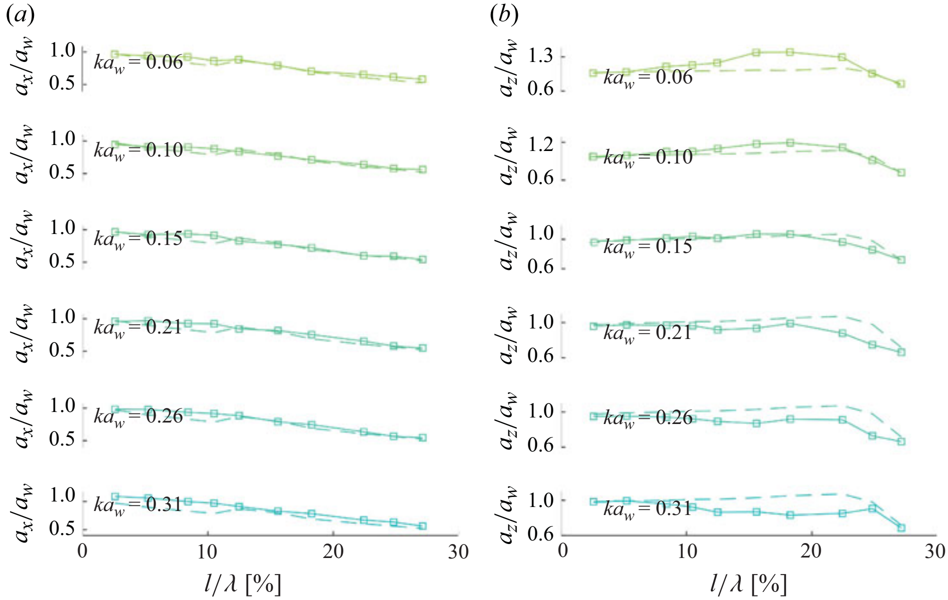

Figure 13. Comparison of the amplitudes of oscillatory motion for objects of different sizes and in different wave steepness from experiments to results predicted by a linear BEM model. (*a*) Horizontal oscillatory motion. (*b*) Vertical oscillatory motion. The motion amplitudes in panels (a) and (b) are normalised by the incident wave amplitude $a_w$. Markers connected by continuous lines correspond to the results from experiments, while dashed lines of the same colour are those from BEM simulations.

As the diffraction-modified Stokes drift (3.3) is calculated based on the linear oscillatory motion of the object, figure 13 compares the amplitudes of the horizontal and vertical components of motion between experiments and the linear BEM that underlies (3.3) (see Xiao *et al.* (2024) for details) as a function of relative size for different values of wave steepness. The linear BEM model performs well in predicting the horizontal oscillatory motions for all objects and wave steepnesses, but fails to accurately predict the vertical motions of larger objects where the assumption of linearity underlying the BEM model probably fails.

Despite the difference in density between the objects used here ($\rho = 636.2\,\mathrm{kg\,m^{-3}}$) and by Harms (1987) ($\rho = 0.92\,\mathrm{kg\,m^{-3}}$), the empirical formula by Harms (1987) still works well for small wave steepness and all object sizes considered here. However, the formula by Harms (1987) underestimates the drift significantly for all sizes when the wave steepness is relatively large ($ka_w \geq 0.16$).

The empirical formula of Harms (1987) is a discontinuous function of $T_w/T_{O,R}$, with one parametric fit for short-period waves, $T_w/T_{O,R} \leq 1.15$ (corresponding to objects of large relative size) and another for long-period waves, $T_w/T_{O,R} > 1.15$ (corresponding to objects of small relative size). The transition from short-wave to long-wave drift behaviour occurs when $T_w/T_{O,R} = 1.15$. According to (3.4), Stokes object drift is fundamentally different in long and short waves. When the object is small, that is, in the long-wave regime, the drift increases monotonically with relative size, while when the object is large, that is, in the short-wave regime (i.e. when $l/\lambda \geq 50\%$) drift decreases continuously with relative size. The drift peaks at the transition point between the two regimes.

Finally, in figures 14 and 15, we present the domains over which the different models we have discussed agree with the experimental data in this paper. When an object is very small $l/\lambda \lesssim 3.2\%$, it is transported at a speed equal to the theoretical Stokes drift for the

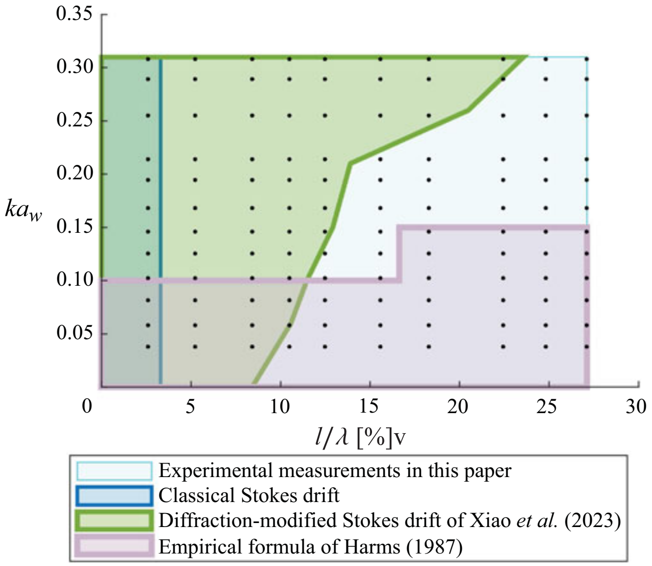

Figure 14. Domains of validity of the three different models for Stokes object drift within the parameter space covered by experiments in this paper: the classical Stokes drift for idealised Lagrangian particles (3.1), the diffraction-modified Stokes drift (3.3), and the empirical formula of Harms (1987) (3.4). The black dot represents the experimental data points.

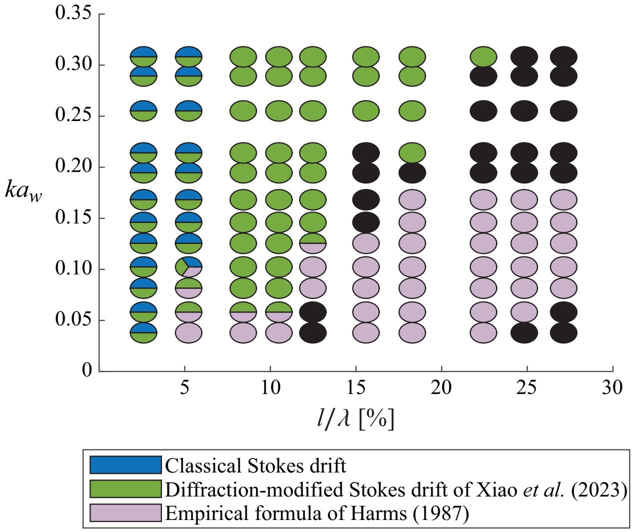

Figure 15. Domain of validity of the three models compared with the experiments in this paper. Each circle represents an experiment, with the colour of the filled circle denoting the model(s) that has an error of less than 20% compared with the experiment. The black circle corresponds to an experiment for which none of the three models is able to predict the drift observed in experiments with an error of less than 20%. Blue and green denote the classical Stokes drift and the diffraction-modified Stokes drift, respectively. Purple denotes the empirical formula of Harms (1987) (3.4). A combination of colours within a circle suggests multiple models have an error of less than 20% compared with experiments.

full range of wave steepness considered. As object size increases, up to $l/\lambda=$ 8.4–23.6% depending on steepness, drift behaviour is enhanced compared with the theoretical Stokes drift, and the diffraction-modified Stokes drift gives a relative error of less than 20% when compared with experimental data. The diffraction-modified Stokes drift predicts drift enhancement as a result of increased vertical motion (relative to the incident wave field) and the difference between the diffracted and radiated wave fields. The range of object sizes for which the diffraction-modified Stokes drift result of Xiao *et al.* (2024) is valid depends on the wave steepness (see figure 11). As the wave steepness increases, its drift enhancement amplification (relative to the theoretical Stokes drift) decreases to a smaller number compared with the same ratio in low wave steepness. As the relative object size is increased further, the assumptions underlying the diffraction-modified Stokes drift derivation by Xiao *et al.* (2024) break down, and the theory becomes ineffective. The empirical formula by Harms (1987) for large object sizes is then more accurate provided the steepness is low. To investigate the correlation between object drift and both relative size and wave steepness, we perform the polynomials regression analysis based on our experimental data. The detailed analysis including our own parametrisation is given in Appendix 4.3.

## 5. Conclusion

This paper has presented an experimental study of the drift of large rectangular 2-D objects under the action of waves and, in doing so, evaluated the effectiveness of the diffraction-modified Stokes drift model proposed by Xiao *et al.* (2024). It is experimentally difficult to examine the drift of 2-D objects (as objects may spin under the influence of lateral variation and become jammed). To overcome these difficulties, we have designed objects that float freely on the water's surface, while occupying the full width of the wave flume used, meaning our experiments are as close to 2-D as possible. To achieve this, the objects are equipped with low-friction bearings and 'flange' structures to support these bearings for small objects.

We have considered rectangular objects with sizes up to 27 % of the length of the incident waves. Very small objects (less than 3 % of the wavelength) essentially behave as Lagrangian tracers, and their drift is well captured by the classical Stokes drift of Stokes (1847). However, for larger objects, we found drift much greater than that predicted by the classical Stokes drift; we observed drift velocities up to 17 times larger than the Stokes drift in the extreme case (for the largest object in the smallest steepness waves considered).

In trying to understand the behaviour of larger objects, an important transition occurs when the ratio of the incident wave period to the natural frequency of heave is of order 1 ($T_w/T_{O,H}=\mathcal{O}(1)$), as previously observed by Harms (1987). Around this point, the vertical oscillatory motion peaks and the drift behaviour changes from increasing with relative size to decreasing with relative size. For objects that are large enough to diffract the wave field and whose natural period of oscillation is significantly smaller than that of the incident waves, the enhanced drift appears to be primarily caused by the disturbance to the wave field the object causes. Xiao *et al.* (2024) proposed a diffraction-modified Stokes drift, which appears to capture the drift behaviour well in this regime. Once the object becomes too large ($\sim l/\lambda > 10\%$), the small-parameter assumption underlying the diffraction-modified Stokes drift starts to break down. The domain of validity of the diffraction-modified Stokes drift extends to larger objects for steeper waves, which we attribute to the fact that the drift enhancement amplification $u_{O,S}/u_S$ is greatly reduced (more linear) for high wave steepness, which, somewhat counter-intuitively, extends the range the underlying linear BEM model is valid.

The transition behaviour is related to the behaviour of the objects' natural heave motion. For objects whose natural period of motion is much smaller than the period of the incoming waves, the oscillatory motion of the object change monotonically (vertically increased and horizontally decreased). The drift increases with object size. The drift enhancement for such objects is attributed by Xiao *et al.* (2024) to increases in their heave motion and a positive imbalance between the effects of the diffracted and radiated wave fields. For objects whose periods are much larger than those of the incoming waves, the oscillatory motions are greatly reduced (e.g. $l/\lambda = 27.1\,\%$), and their drift increases with relative size at a slow rate or becomes constant.

The dependence of drift behaviour on wave steepness is found not to be purely quadratic (as predicted by Stokes (1847)) but a mixture of linear and quadratic, and changing with relative size. In addition, if the waves are too steep, the linearised BEM model we use to predict diffraction, and thus the diffraction-modified Stokes drift of Xiao *et al.* (2024), breaks down, and a higher-order model would be needed to predict the diffracted and radiated wave field. The empirical formula of Harms (1987) does well for larger object sizes and small steepness, but breaks down for larger steepness. Based on our experimental data, we proposed a new parameterisation that predicts the wave-induced drift as a function of relative size (the ratio of object size to the wavelength) and wave steepness, including linear and quadratic terms.

We make the following four recommendations for future work. First, the diffraction-modified Stokes drift model of Xiao *et al.* (2024) should be made suitable for more nonlinear circumstances by expanding (3.3), which is based on small-parameter assumptions and only retains first-order terms, to include higher-order terms. Due to the linearity of the BEM model used to calculate the radiated and diffracted wave fields and the approximate nature of the model, the diffraction-modified Stokes drift theory based on (3.3) from Xiao *et al.* (2024) is ineffective in predicting the drift for large objects in high wave steepness.

Second, while (second-order) drift forces are routinely calculated (e.g. Newman (1967); Faltinsen (1993)), it remains unclear how a force balance (between the drift force and the wave drift damping force (Nossen *et al.* 1991; Aranha 1994)) can be used to predict an enhanced steady drift of large objects analogous to the diffraction-modified Stokes drift of Xiao *et al.* (2024). This should be explored in future work.

Third, for ocean waves, including both internal and surface waves, the Lagrangian-mean object drift is given by $\overline{u}_{L,O} = u_{S,O} + \overline{u}_{E,O}$ (e.g., Haney & Young 2017; Van den Bremer & Breivik 2018; Thomas, Bühler & Smith 2018; Higgins, van Den Bremer & Vanneste 2020*a*). To examine the extent to which the Lagrangian-mean object drift is affected by the introduction of finite object size, we have exclusively examined how the Stokes object drift is affected by the finite size of the object, leaving the Eulerian-mean flow unaffected (as in the deep-water diffraction-modified Stokes drift model of Xiao *et al.* (2024)). Under certain circumstances, it is not inconceivable that the Eulerian-mean flow may also be affected by the presence of the object, when this becomes very large and prohibits fluid passage. This could result in flow blockage; the Eulerian-mean flow would exhibit a distinctly different structure compared with that assumed in the current study.

We hypothesise that the effect of finite object size on the Eulerian-mean flow field is more evident in shallow water depths, where the contribution of the second-order velocity potential to drift cannot be neglected (Pessoa & Fonseca 2015). Therefore, we recommend the effects of finite depth to be examined in future work.

Fourth, although the focus of this paper has been on two-dimensional geometries, we acknowledge that such a configuration is a very strong simplification of wave-induced drift in many real-world environments. Future work is thus recommended to explore how the

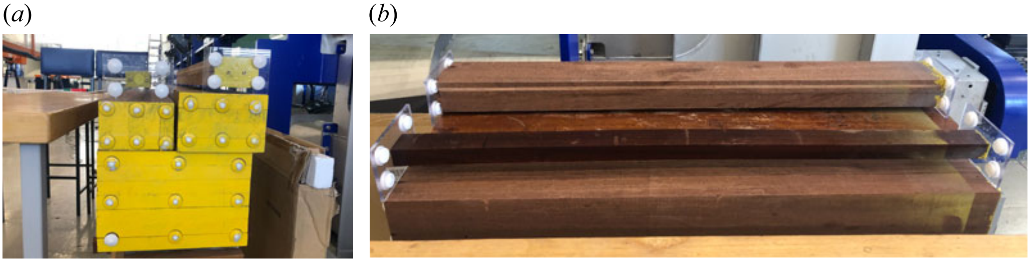

Figure 16. Two-dimensional-type objects. (*a*) Side view of five objects (painted yellow) installed with bearings. Objects 1, 2, 3, 4 and 5 are shown from left to right, top to bottom. Objects 1 and 2 are designed with 'flange' structure shown in figure 2. (*b*) Front view of objects.

presence of a third dimension and the influence of object width affect the diffraction-modified Stokes drift mechanism. As diffraction of the wave field is the main cause of enhanced drift, we expect drift enhancement to be reduced in 3-D compared with 2-D for a unidirectional incident wave field, as waves can diffract around the object in 3-D instead of just being either reflected or transmitted (2-D). Finally, it would be of interest to explore the effects of directional spreading.

**Acknowledgements.** Q.X. is supported by the China Scholarship Council-PAG Oxford Scholarship. T.S.vdB was supported by a Royal Academy of Engineering Research Fellowship.

**Declaration of interests.** The authors report no conflict of interest.

**CRediT author statement.** Qian Xiao: Conceptualisation, experimental design and execution, data collection and analysis, writing-original draft preparation. Mark McAllister: Experimental design, supervision, writing-reviewing and editing. Tom Adcock: conceptualisation, supervision, writing-reviewing and editing. Ton van den Bremer: conceptualisation, supervision, writing-reviewing and editing.

## Appendix A. Photographs of objects with bearings

Figure 16 provides side and front views of the objects outside of the water. It shows the yellow-painted ends of the objects, where the bearings are installed.

## Appendix B. Measurement error and repeatability

To assess the repeatability of the experiments we present and the precision of the approaches we use to acquire measurements, we performed repeated experiments for four wave steepnesses ($ka_w = 0.06$, 0.10, 0.20 and 0.32) for each object size $l/\lambda$. We conducted five repeats for these experiments and present the results in figure 17, where we show normalised linear oscillatory motions and drift as a function of relative size for different wave steepness. For drift, our experiments demonstrate very small variability for low wave steepness and small objects; variability is larger for high wave steepness and larger objects. We attribute this to two factors. Firstly, the way we conducted the experiment plays a role. For very small objects in low wave steepness, we limited the object to drift a shorter section of the flume (only the middle two sections, 4 m) instead of allowing it to drift along the entire length. This is because these objects travel very slowly. The objects are thus not subject to any potential variation in conditions along the length of the flume, leading to less variability. However, for larger objects in high wave steepness, which travel more quickly, for one experiment, we needed to perform 2–3 runs to ensure that we acquired sufficient data for at least 35 wave periods (after reaching a quasi-steady state). This introduces more variability in the measurements. The second factor that contributes to the variability is the repeatability of the waves in the flume, as shown in figure 18. The variability of

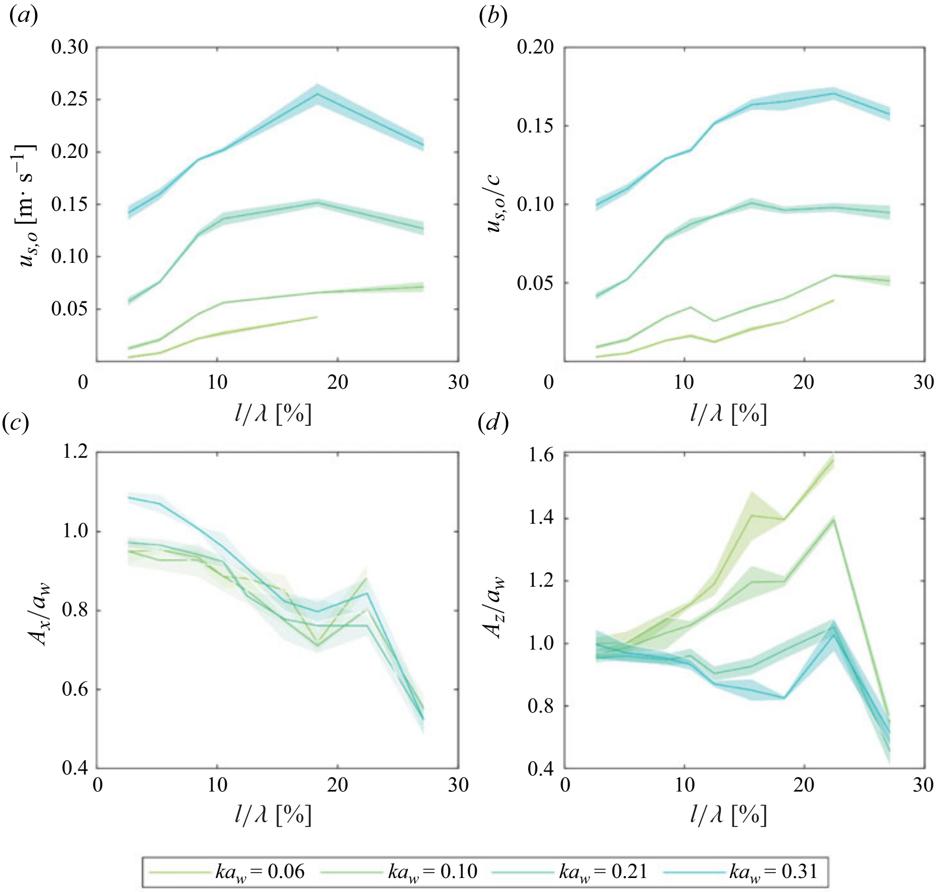

Figure 17. Uncertainty envelopes as a function of relative size for different wave steepness: (*a*) Stokes object drift, these data are shown without normalisation, and we only plot data for objects with relative sizes of $l/\lambda = 2.6\%$, 5.2%, 8.4%, 10.5%, 18.3% and 27.1%; (*b*) celerity-normalised Stokes object drift velocity; (*c*) wave-amplitude-normalised magnitude of horizontal motion; (*d*) wave-amplitude-normalised magnitude of vertical motion. Mean values, denoted by lines, are obtained using five repeat experiments. The error bars, shown as shaded areas, correspond to two standard deviations either side of the mean. The transparency of panel (*c*) has been adjusted to make it clearer for overlapping parts.

the oscillatory motion appears larger due to the normalisation process, where the standard deviation is amplified. Unlike the drift, the relatively large variability of the oscillatory motions occurs primarily in cases with small objects and intermediate wave steepness. Apart from the wave repeatability and ways to conduct the experiment, this is also due to the fact that the larger the object is, the easier it is to capture its bobbing motion using the camera.

We assess the repeatability of the waves in the absence of the object here, to better understand the nature of the uncertainty we observe above. The wave gauges set up are the same as in § 2.1. We chose four wave steepnesses ($ka_w = 0.06$, 0.10, 0.20 and 0.32) for each frequency in table 2. We conducted five repeats for each experiment. The mean values of wave amplitude for each wave gauge are calculated, and we use the average value of all seven gauges as our wave amplitude for one repeat. The measured data are given in figure 18. The main variability occurs at high wave steepness, and at intermediate wave steepness for a frequency of $f = 1.1$ Hz. This variability is most likely caused by

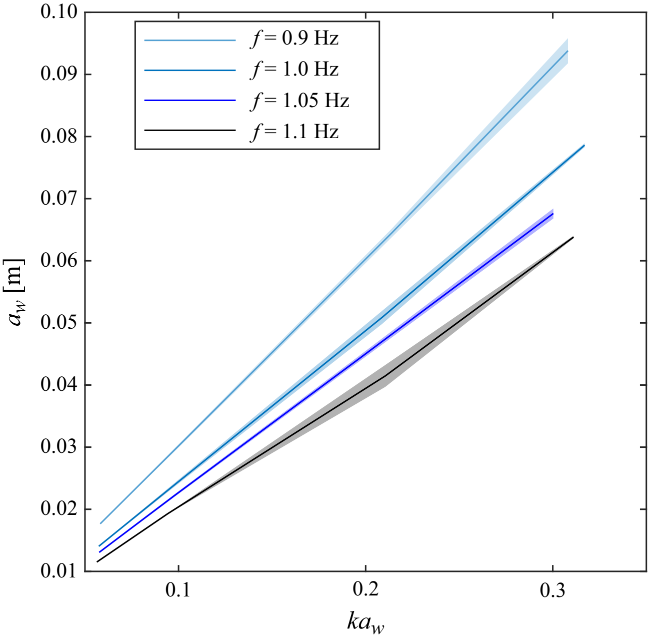

Figure 18. Uncertainty envelopes of wave amplitude as a function of wave steepness for different wave frequencies. Mean values, denoted by lines, are obtained using five repeated experiments. The error bars, shown as shaded areas, correspond to two standard deviations either side of the mean.

| | $l/\lambda = 2.6\%$ | | $l/\lambda = 12.5\%$ | | $l/\lambda = 22.4\%$ | |
|---|---|---|---|---|---|---|
| $ka_w$ | 1-$R^2$ | $\sigma/\overline{u}_{L,O}$ | 1-$R^2$ | $\sigma/\overline{u}_{L,O}$ | 1-$R^2$ | $\sigma/\overline{u}_{L,O}$ |
| 0.06 | 0.012 | 0.0083 | 0.011 | 0.0015 | 0.009 | 0.0029 |
| 0.10 | 0.023 | 0.0054 | 0.015 | 0.0011 | 0.014 | 0.0094 |
| 0.21 | 0.046 | 0.0056 | 0.029 | 0.0140 | 0.025 | 0.0067 |
| 0.31 | 0.074 | 0.0130 | 0.043 | 0.0042 | 0.040 | 0.0151 |

Table 8. Measurement error of the Lagrangian object drift $\overline{u}_{L,O}$ during fitting of the horizontal trajectory for objects with different sizes and in varying wave steepness. We chose three different sizes of objects to report here: $l/\lambda = 2.6\%$ for Object 1 in wave $f = 0.9$ Hz ; $l/\lambda = 12.5\%$ for Object 3 in wave $f = 1.1$ Hz ; $l/\lambda = 22.4\%$ for Object 5 in wave $f = 1.0$ Hz. $1 - R^2$ refers to the goodness of fit with $R^2$ the uncertainty in the prediction of the fitted polynomial. $\sigma$ refers to the standard deviation (uncertainty of the coefficients) of the linear coefficient determination in the fit, and thus $\sigma/\overline{u}_{L,O}$ represents the standard deviation of the fitted linear coefficient.

reflections that are not absorbed by the beach. We conclude wave gauge measurements are a small cause of error.

We calculate drift velocity by performing a linear regression on the measured trajectories once a steady state is reached. To evaluate how well this works for our measured object trajectories and estimate the uncertainty in the gradient (drift velocity, $\overline{u}_{L,O}$), we report the measurement errors, including the coefficients of determination in table 8. The quantity $1 - R^2$ increases monotonically with wave steepness. This is expected, as larger wave steepness leads to larger horizontal oscillatory motions of the object, causing deviations from a constant gradient and increasing the uncertainty in the fit. The relative uncertainties for the parameters are all very small with a maximum value of 1.5 %.

## REFERENCES

ALSINA, J., JONGEDIJK, C.E. & VAN SEBILLE, E. 2020 Laboratory measurements of the wave-induced motion of plastic particles: influence of wave period, plastic size and plastic density. *J. Geophys. Res. Oceans* **125** (12), e2020JC016294.

ARANHA, J.A.P. 1994 A formula for wave damping in the drift of a floating body. *J. Fluid Mech.* **275**, 147–155.

ARIKAINEN, A.I. 1972 Wave drift of an isolated floe. *AIDJEX Bulletin* **1** (16), 125–131.

BANIELA, S. I. 2008 Roll motion of a ship and the roll stabilising effect of bilge keels. *J. Navig.* **61** (4), 667–686.

BOULLUEC, M.LE, FOREST, B. & MANSUY, E. 2008 Steady drift of floating objects in waves: experimental and numerical investigation. In *International Conference on Offshore Mechanics and Arctic Engineering*, vol. 48210, pp. 321–328.

BREIVIK, Ø., ALLEN, A.A., MAISONDIEU, C. & OLAGNON, M. 2013 Advances in search and rescue at sea. *Ocean Dyn.* **1** (63), 83–88.

BÜHLER, O. 2014 *Waves and Mean Flows*. 2nd edn. Cambridge University Press.

CALVERT, R., MCALLISTER, M.L., WHITTAKER, C., RABY, A., BORTHWICK, A.G.L. & VAN DEN BREMER, T.S. 2021 A mechanism for the increased wave-induced drift of floating marine litter. *J. Fluid Mech.* **915**, A73.

CARLTON, J.T. *et al.* 2018 Ecological and biological studies of ocean rafting: Japanese tsunami marine debris in North America and the Hawaiian Islands. *Aquat. Invasions* **13** (1), 1–9.

CHEN, X.B. 2007 Middle-field formulation for the computation of wave-drift loads. *J. Engng Math.* **59** (1), 61–82.

CÓZAR, A., *et al.* 2014 Plastic debris in the open ocean. *Proc. Natl Acad. Sci.* **111** (28), 10239–10244.

DEBOK, D. & ROEHRIG, S. 1981 Numerical modelling of coast guard buoys in shallow water. In *OCEANS 81*, pp. 174–179. IEEE.

DEIKE, L., PIZZO, N. & MELVILLE, W.K. 2017 Lagrangian transport by breaking surface waves. *J. Fluid Mech.* **829**, 364–391.

DIBENEDETTO, M.H., CLARK, L.K. & PUJARA, N. 2022 Enhanced settling and dispersion of inertial particles in surface waves. *J. Fluid Mech.* **936**, A38.

DIBENEDETTO, M.H., KOSEFF, J.R. & OUELLETTE, N.T. 2019 Orientation dynamics of nonspherical particles under surface gravity waves. *Phys. Rev. Fluids* **4** (3), 034301.

DIBENEDETTO, M.H. & OUELLETTE, N.T. 2018 Preferential orientation of spheroidal particles in wavy flow. *J. Fluid Mech.* **856**, 850–869.

DIBENEDETTO, M.H., OUELLETTE, N.T. & KOSEFF, J.R. 2018 Transport of anisotropic particles under waves. *J. Fluid Mech.* **837**, 320–340.

DOBLER, D., HUCK, T., MAES, C., GRIMA, N., BLANKE, B., MARTINEZ, E. & ARDHUIN, F. 2019 Large impact of Stokes drift on the fate of surface floating debris in the South Indian Basin. *Mar. Pollut. Bull.* **148**, 202–209.

EAMES, I. 2008 Settling of particles beneath water waves. *J. Phys. Oceanogr.* **38** (12), 2846–2853.

EELTINK, D., CALVERT, R., SWAGEMAKERS, J.E., XIAO, Q. & VAN DEN BREMER, T.S. 2023 Stochastic particle transport by deep-water irregular breaking waves. *J. Fluid Mech.* **971**, A38.

EI-TAHAN, M.S., EI-TAHAN, H.W., VENKATESH, S., *et al.* 1983 Forecast of iceberg ensemble drift. In *Offshore Technology Conference. Offshore Technology Conference*,

ERIKSEN, M., LEBRETON, L.C.M., CARSON, H.S., THIEL, M., MOORE, C.J., BORERRO, J.C., GALGANI, F., RYAN, P.G. & REISSER, J. 2014 Plastic pollution in the world's oceans: more than 5 trillion plastic pieces weighing over 250,000 tons afloat at sea. *PloS One* **9** (12), e111913.

FALTINSEN, O. 1993 *Sea Loads On Ships and Offshore Structures*. Cambridge Ocean Technology Series. Volume 1. Cambridge University Press.

GODA, Y. & SUZUKI, Y. 1976 Estimation of incident and reflected waves in random wave experiments. In *Coastal Engineering*, pp. 828–845. Coastal Engineering Research Council.

GROTMAACK, R. & MEYLAN, M.H. 2006 Wave forcing of small floating bodies. *J. Waterways Port Coast. Ocean Engng* **132** (3), 192–198.

HANEY, S. & YOUNG, W.R. 2017 Radiation of internal waves from groups of surface gravity waves. *J. Fluid Mech.* **829**, 280–303.

HARMS, V.W. 1987 Steady wave-drift of modeled ice floes. *J. Waterw. Port C* **113** (6), 606–622.

HASKIND, M.D. 1946 The hydrodynamic theory of ship oscillations in rolling and pitching. *Prikl. Mat. Mech.* **10**, 33–66.

HAVELOCK, T.H. 1909 The wave-making resistance of ships: a theoretical and practical analysis. *Proc. R. Soc. Lond. A-Math. Phy.* **82** (554), 276–300.

HAVELOCK, T.H. 1942 The drifting force on a ship among waves. *Lond. Edinburgh, and Dublin Phil. Mag. J. Sci.* **33** (221), 467–475.

HE, M., REN, B. & QIU, D. 2016 Experimental study of nonlinear behaviors of a free-floating body in waves. *Chin. Ocean Engng* **30** (3), 421–430.

HIGGINS, C., VAN DEN BREMER, T.S. & VANNESTE, J. 2020*a* Lagrangian transport by deep-water surface gravity wavepackets: effects of directional spreading and stratification. *J. Fluid Mech.* **883** (A42),

HIGGINS, C., VANNESTE, J. & VAN DEN BREMER, T.S. 2020*b* Unsteady Ekman-Stokes dynamics: implications for surface wave-induced drift of floating marine litter. *Geophys. Res. Lett.* **47** (18), e2020GL089189.

HUANG, G., HUANG, Z.H. & LAW, A.W. 2016 Analytical study on drift of small floating objects under regular waves. *J. Eng. Mech.* **142** (6), 06016002.

HUANG, G., LAW, A.W. & HUANG, Z. 2011 Wave-induced drift of small floating objects in regular waves. *Ocean Engng* **38** (4), 712–718.

HUANG, G. & LAW, A.W.K. 2013 Wave-induced drift of large floating objects in regular waves. *J. Waterways Port Coast. Ocean Engng* **139** (6), 535–542.

ISAACSON, M.D. 1979 Wave-induced forces in the diffraction regime. In *Mechanics of Wave-Induced Forces on Cylinders* (ed. T.L.SHAW), pp. 68–89. Pitman Publishing, Ltd.

IWASAKI, S., ISOBE, A., KAKO, S., UCHIDA, K. & TOKAI, T. 2017 Fate of microplastics and mesoplastics carried by surface currents and wind waves: a numerical model approach in the Sea of Japan. *Mar. Pollut. Bull.* **121** (1-2), 85–96.

LAW, K.L. 2017 Plastics in the marine environment. *Annu. Rev. Mar. Sci.* **9** (1), 205–229.

LAW, K.L., MORÉT-FERGUSON, S., MAXIMENKO, N.A., PROSKUROWSKI, G., PEACOCK, E.E., HAFNER, J. & REDDY, C.M. 2010 Plastic accumulation in the North Atlantic subtropical gyre. *Science* **329** (5996), 1185–1188.

LEFEVRE, J.M. & COTTON, P.D. 2001 Ocean surface waves. In *International Geophysics*, vol. 69, pp. 305–xix. Elsevier.

LENAIN, L., PIZZO, N. & MELVILLE, W.K. 2019 Laboratory studies of Lagrangian transport by breaking surface waves. *J. Fluid Mech.* **876**, R1. https://doi.org/10.1017/jfm.2019.544.

LONGUET-HIGGINS, M.S. 1953 Mass transport in water waves. *Phil. Trans. R. Soc. A* **245** (903), 535–581.

MANSARD, E.P.D. 1980 The measurement of incident and reflected spectra using least square method. In *Proc. 17th Coastal Eng.*, Sydney, Australia, vol. 1, pp. 154–172.

MAXEY, M.R. & RILEY, J.J. 1983 Equation of motion for a small rigid sphere in a non-uniform flow. *Phys. Fluids* **26** (4), 883–889.

MEYLAN, M.H., YIEW, L.J., BENNETTS, L.G., FRENCH, B.J. & THOMAS, G.A. 2015 Surge motion of an ice floe in waves: comparison of a theoretical and an experimental model. *Ann. Glaciol.* **56** (69), 155–159.

MICHELL, J.H., XI 1898 The wave-resistance of a ship. *Lond. Edinburgh, and Dublin Phil. Mag. J. Sci.* **45** (272), 106–123.

MONISMITH, S.G. 2020 Stokes drift: theory and experiments. *J. Fluid Mech.* **884**, F1.

MORISON, J.R., JOHNSON, J.W. & SCHAAF, S.A. 1950 The force exerted by surface waves on piles. *J. Petrol. Technol.* **2** (05), 149–154.

MURRAY, J., GUY, G. & MUGGERIDGE, D. 1983 Response of modelled ice masses to regular waves and regular wave groups. In *Proceedings OCEANS'83*, pp. 1048–1052. IEEE.

NATH, J.H. 1978 Drift speed of buoys in waves. *Coast. Engng Proc.* **1** (16), 49–49.

NEWMAN, J.N. 1967 The drift force and moment on ships in waves. *J. Ship Res.* **11** (01), 51–60.

NEWMAN, J.N. 2018 *Marine Hydrodynamics*. MIT Press.

NOSSEN, J., GRUE, J. & PALM, E. 1991 Wave forces on three-dimensional floating bodies with small forward speed. *J. Fluid Mech.* **227**, 135–160.

PERRIE, W. & HU, Y. 1997 Air–ice–ocean momentum exchange. Part II: ice drift. *J. Phys. Oceanogr.* **27** (9), 1976–1996.

PESSOA, J. & FONSECA, N. 2015 Second-order low-frequency drift motions of a floating body calculated by different approximation methods. *J. Mar. Sci. Technol.* **20** (2), 357–372.

PINKSTER, J.A. & HOOFT, J.P. 1976 Low frequency second order wave forces on vessels moored at sea. In *11th Symposium on Naval Hydrodynamics*. ONR, London, England.

PINKSTER, J.A. & VAN OORTMERSSEN, G. 1977 Computation of the first and second order wave forces on bodies oscillating in regular waves. In *2nd International Conference on Numerical Ship Hydrodynamics*, pp. 136–456.

PIZZO, N., MELVILLE, W.K. & DEIKE, L. 2019 Lagrangian transport by nonbreaking and breaking deep-water waves at the ocean surface. *J. Phys. Oceanogr.* **49** (4), 983–992.

PUJARA, N. & THIFFEAULT, J. Jul 2023 Wave-averaged motion of small particles in surface gravity waves: effect of particle shape on orientation, drift, and dispersion. *Phys. Rev. Fluids* **8** (7), 074801. https://doi.org/10.1103/PhysRevFluids.8.074801

REN, B., HE, M., DONG, P. & WEN, H. 2015 Nonlinear simulations of wave-induced motions of a freely floating body using WCSPH method. *Appl. Ocean Res.* **50**, 1–12.

RÖHRS, J., CHRISTENSEN, K.H., HOLE, L.R., GÖ. BROSTRÖM, M.D. & SUNDBY, S. 2012 Observation-based evaluation of surface wave effects on currents and trajectory forecasts. *Ocean Dyn.* **62** (10–12), 1519–1533.

RUMER, R.R., CRISSMAN, R.D. & WAKE, A. 1979 *Ice Transport in Great Lakes*. Great Lakes Environmental Research Laboratory, National Oceanic and Atmospheric Administration.

SANTAMARIA, F., BOFFETTA, G., AFONSO, M.M., MAZZINO, A., ONORATO, M. & PUGLIESE, D. 2013 Stokes drift for inertial particles transported by water waves. *EPL (Europhysics Letters)* **102** (1), 14003.

SETÄLÄ, O., FLEMING-LEHTINEN, V. & LEHTINIEMI, M. 2014 Ingestion and transfer of microplastics in the planktonic food web. *Environ. Pollut.* **185**, 77–83.

SHEN, H.H. & ACKLEY, S.F. 1991 A one-dimensional model for wave-induced ice-floe collisions. *Ann. Glaciol.* **15**, 87–95.

SHEN, H.H. & ZHONG, Y. 2001 Theoretical study of drift of small rigid floating objects in wave fields. *J. Waterways Port Coast. Ocean Engng* **127** (6), 343–351.

SINNIS, J.T., GRARE, L., LENAIN, L. & PIZZO, N. 2021 Laboratory studies of the role of bandwidth in surface transport and energy dissipation of deep-water breaking waves. *J. Fluid Mech.* **927**, A5. https://doi.org/10.1017/jfm.2021.734.

SKEJIC, R. & FALTINSEN, O.M. 2008 A unified seakeeping and maneuvering analysis of ships in regular waves. *J. Mar. Sci. Technol.* **13** (4), 371–394.

STOKES, G.G. 1847 On the theory of oscillatory waves. *Trans. Camb. Phil. Soc.* **8**, 411–455.

SUYEHIRO, K. 1924 The drift of ships caused by rolling among waves. *Trans. Inst. Naval Arch.* **66**, 4998.

TANIZAWA, K., MINAMI, M. & IMOTO, Y. 2001 On the drifting speed of floating bodies in waves. *J. Soc. Nav. Archit. Japan* **2001** (190), 151–160.

THOMAS, J., BÜHLER, O. & SMITH, K.S. 2018 Wave-induced mean flows in rotating shallow water with uniform potential vorticity. *J. Fluid Mech.* **839**, 408–429.

TOFFOLI, A. & BITNER-GREGERSEN, E.M. 2017 Types of ocean surface waves, wave classification. In *Encyclopedia of Maritime and Offshore Engineering* (eds J. Carlton, P. Jukes & Y.S. Choo), pp. 1–8. https://doi.org/10.1002/9781118476406.emoe077.

VAN DEN BREMER, T.S. & BREIVIK, Ø. 2018 Stokes drift. *Philos. T. Roy. Soc. A* **376** (2111), 20170104.

VAN DEN BREMER, T.S. & TAYLOR, P.H. 2015 Estimates of lagrangian transport by surface gravity wave groups: the effects of finite depth and directionality. *J. Geophys. Res. Oceans* **120** (4), 2701–2722.

VAN DEN BREMER, T.S. & TAYLOR, P.H. 2016 Lagrangian transport for two-dimensional deep-water surface gravity wave groups. *P. Roy. Soc. A-Math. Phy* **472** (2192), 20160159.

VAN SEBILLE, E. *et al.* 2020 The physical oceanography of the transport of floating marine debris. *Environ. Res. Lett.* **15** (2), 023003.

VAN SEBILLE, E., WILCOX, C., LEBRETON, L., MAXIMENKO, N., HARDESTY, B.D., VAN FRANEKER, J.A., ERIKSEN, M., SIEGEL, D., GALGANI, F. & LAW, K.L. 2015 A global inventory of small floating plastic debris. *Environ. Res. Lett.* **10** (12), 124006.

WADHAMS, P. 1983 A mechanism for the formation of ice edge bands. *J. Geophys. Res. Oceans* **88** (C5), 2813–2818.

WATANABE, Y. 1938 Some contributions of the theory of rolling. *Trans. Inst. Naval Arch.* **80**, 408–432.

WILSON, W. 1982 Numerical modelling of drifting buoys and its relevance to Lagrangian tracking. In *Proceedings of the 1982 IEEE Second Working Conference on Current Measurement*, vol. 2, pp. 95–97. IEEE.

XIAO, Q., CALVERT, R., YAN, S.Q., ADCOCK, T.A.A. & VAN DEN BREMER, T.S. 2024 Surface gravity wave-induced drift of floating objects in the diffraction regime. *J. Fluid Mech.* **980**, A27.

XIE, S. 2015 Code for holistically-nested edge detection and pretrained model. Available at https://github.com/s9xie/hed, Last accessed on 2023-3-30.

XIE, S. & TU, Z. 2015 Holistically-nested edge detection. In *Proceedings of the IEEE International Conference on Computer Vision*, pp. 1395–1403.